

The University of Texas at Austin



Final Report

Precision Machine Design of a Lathe

Zuhair Farra

Phillip Gavino

Clay McPherson

Luis Moncada

Pranay Srivastava

Anastasia Timoshenko

M E 392M 9: Precision Machine Design

Dr. Michael Cullinan

December 11, 2023

Table of Contents

Table of Contents	1
1. Introduction.....	1
2. Subassemblies and Components	1
2.1. Spindle.....	1
2.1.1. Bearings Selection	1
2.1.2. Spindle Model.....	1
2.2. Flexures	3
2.2.1. Flexure Models	4
2.2.2. Flexure Finite Element Analyses	6
2.3. Belt and Pulleys.....	13
2.3.1. Belt and Pulleys Selection	14
2.3.2. Belt and Pulleys Model.....	14
2.3.3. Belt and Pulleys Assembly	16
3. Manufacturing	17
4. Error Model.....	17
4.1. Spindle Loop	18
4.2. Tool Loop	20
5. Metrology.....	24
5.1. Spindle Runout	24
6. Performance	27
7. Conclusion	28
7.1. Improvements	28
Appendix A.....	30
Appendix B.....	36
Appendix C.....	38
Appendix D.....	45

1. Introduction

“A precision machine is an integrated system that relies on the attributes of one component to augment the weaknesses of another component” (Slocum, 1992). This quote above tells what a precision machine actually is, a system that has components relying upon one another. This philosophy was illustrated in the semester-long project for this course, something that integrated many machine elements, analysis methods, and simulations to achieve the best working lathe. Some of the machine element components we learned and integrated in our project were shafts, bearings, flexures, belts and pulleys, power screws, and bolted joints. The methods for analysis for these components were static and fatigue analyses and for the whole system, error modeling was utilized. Simulations such as finite element analysis (FEA) for both static load and modal options. All of these aspects combine together to create an ideal precision machine. In this report, we will explain the different subassemblies and components the team focused on, the error modeling of the system, the metrology, performance, and lastly improvements for a future lathe.

2. Subassemblies and Components

2.1. Spindle

The spindle is the subassembly responsible for holding the work and rigidly stabilizing it while it is subjected to the cutting forces at a high rotational speed. It is driven by the motor via belts and pulleys, transferring the input torque into the work during the cut. The spindle must use specialized bearings to withstand a combination of axial and radial load applied by the tool.

2.1.1. Bearings Selection

The reason that our team chose to select Tapered Roller bearings is that as the compression forces are applied to our spindle from the chuck we wanted to protect and distribute the forces from our shaft to our housing, a stronger structure, to prevent bending in the shaft. Due to us picking tapered bearings we needed to make sure to be able to apply the proper amount of preload force to the system to do so, we simply added two shoulders, one on the housing and one on the shaft to apply pressure to the chuck side bearing. For the pulley side bearing we used a combination of a spring washer and a nut to apply pressure to the bearing against its respective shoulder.

2.1.2. Spindle Model

Below is Figure 1 which shows an angled view of the spindle assembly with the transparent housing.

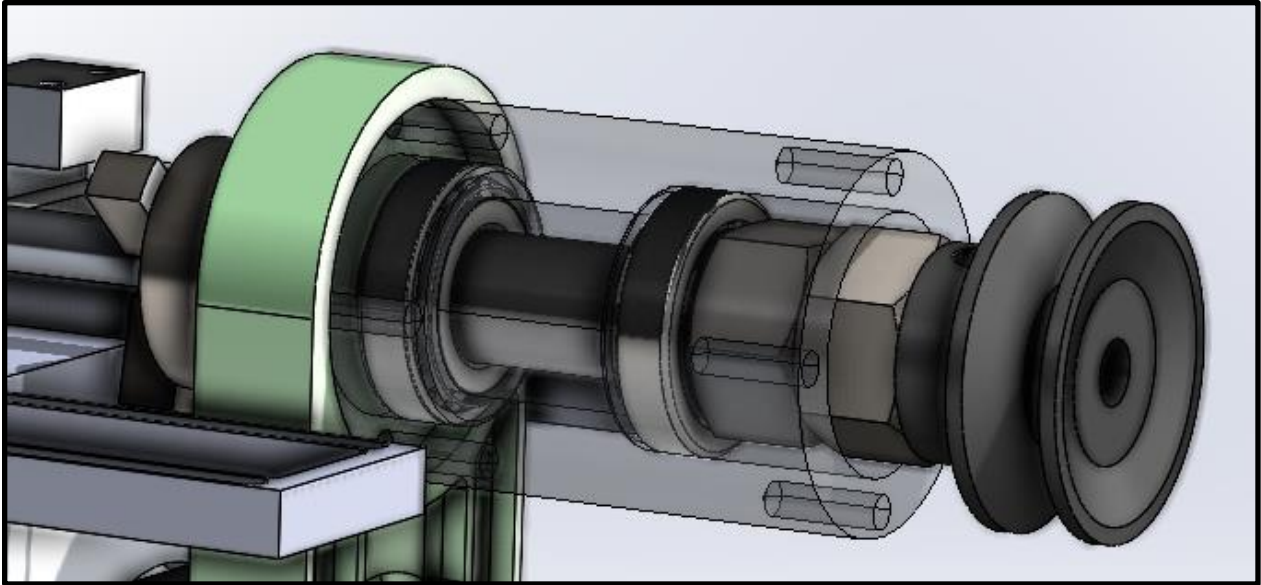


Figure 1. Image of the full spindle assembly.

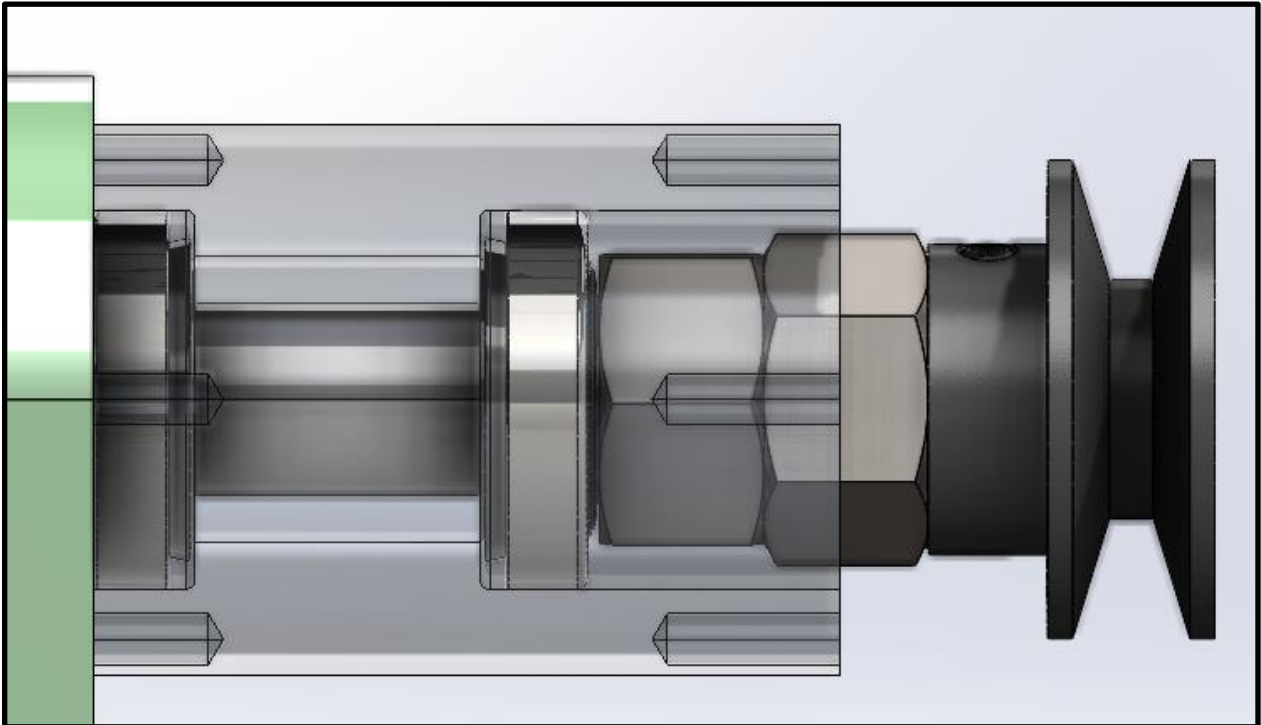


Figure 2. Side view of the spindle assembly.

2.1.3. Spindle Assembly

The spindle was designed for a precise press fit interface with the bearings. This was achieved by allowing approximately 0.0005” of diametric interference between the spindle OD and the race ID. The final dimension was achieved by incrementally sanding the face at low speed while checking the dimension with micrometers.

The two bearings each facing opposite directions axially constrain the part in one direction. This is so that the tightening of the preload nut pulls both inner races inward against their respective outer races which are butted against a step in the housing. The shaft is not stepped on the side with the preload nut and spring, accommodating very small thermal expansions as the spindle moves a few microns to tenths relative to the inner bearing race. The opposite end of the shaft is stepped to sandwich the chuck side bearing between this step and the housing as the preload nut is tightened. If both sides of the spindle were stepped, the assembly would be overconstrained, causing at least one bearing to always be loose due to slight imperfections in geometry.

The chosen preload nut was later found to be excessively large, causing great difficulty in the spindle fabrication due to the extreme forces required to drive the die while cutting the threads. The torque on the preload nut was not so high as to necessitate the strength of such a large thread diameter; a smaller size would’ve significantly simplified the machining and assembly.

2.2. Flexures

The lathe included 3 flexures to act as linear bearings or mounts that do not overconstrain motion. The cross-slide flexure allowed the tool post to move into and out of the part along a single axis while providing rigidity in all other directions. The leadscrew flexure was threaded to mate with the leadscrew itself, driving the carriage forward and back with the z-axis dial. This flexure allowed the carriage to be driven by an imperfect lead screw, accommodating slight bows. The final flexure mounted the carriage to one of the guide rails so that the linear motion was not overconstrained and slight rail misalignment could be tolerated. These flexures are an example of how our precision machine uses some attributes of components to counter the weaknesses of other

components. All flexures were waterjet from Aluminum 7050 stock, with a conservative yield strength of 68000 psi. Flexible portions of the flexures were cut with a temporary fixture tab. This prevented portions of the part from moving during the cut. The temporary tabs were later cut with a hacksaw. Critical hole dimensions were finalized with reamers when the accuracy of the waterjet cut was deemed insufficient for a hole to be tapped, press fit, or otherwise precisely mated to another component.

2.2.1. Flexure Models

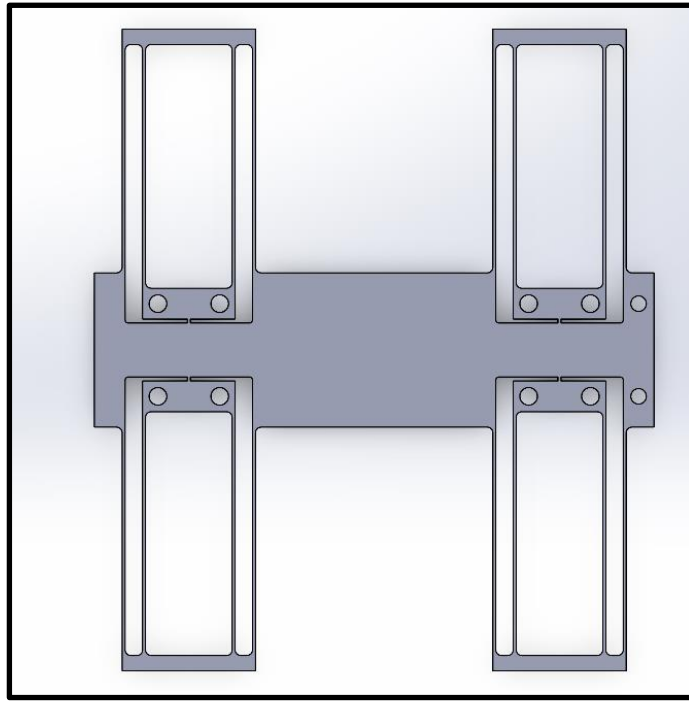


Figure 3: Cross Slide Flexure

The figure above shows the design for the cross slide flexure. This general design is typical for linear bearing flexures of this type. It includes through holes for the bolt pattern of the carriage it is mounted to, and also the mounting block for the dial. This flexure allows for 0.56" of travel along its movement axis, more than sufficient for the full 0.125" depth of cut that the lathe is designed for.

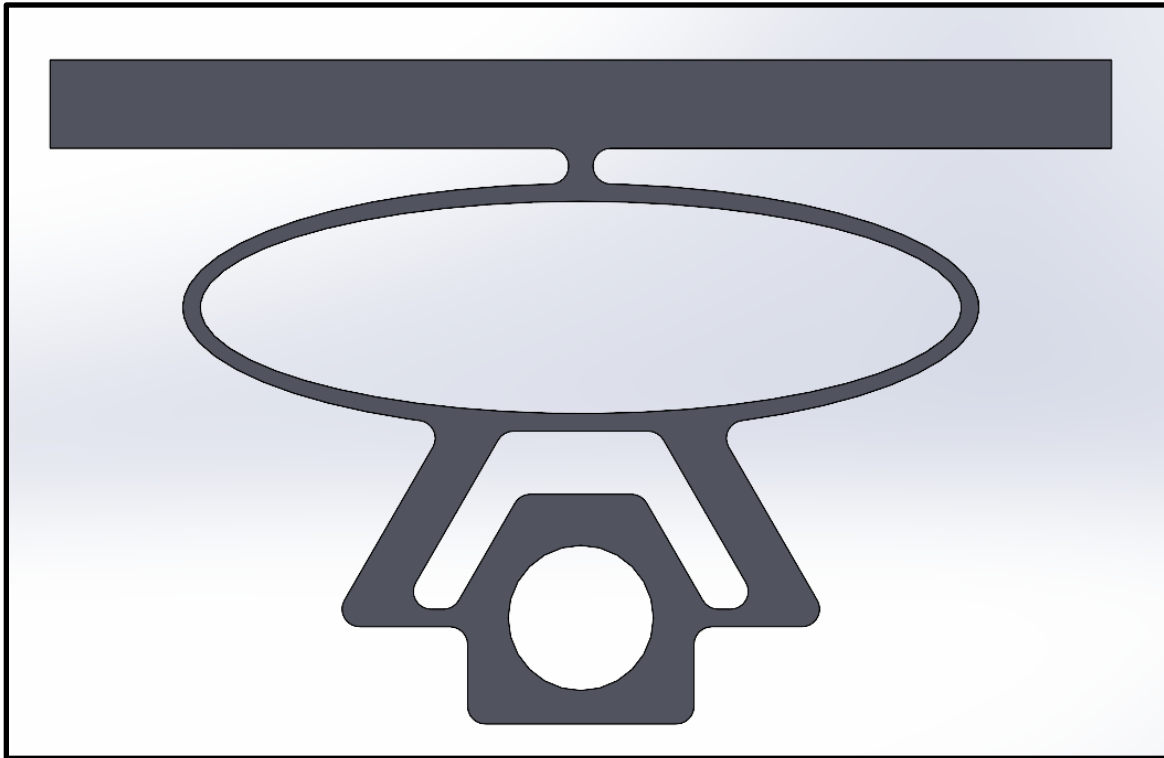


Figure 4: Lead Screw Flexure

The lead screw flexure, pictured above, is designed for rigidity along the intended axis of motion and sufficient freedom of movement to tolerate a slightly non-straight lead screw. The narrow vertical section at the top allows for a slight side to side roll. Combined with the vertical flexibility of the large oval section, this allows the leadscrew to be slightly out of position in any direction along the x and y axis, where z is out of the page as pictured above. The thin horizontal blades on either side of the circular feature which was tapped for the screw allow for bending upward and downward. The thin blade above the oval at the top allows for twisting about its axis, allowing the leadscrew to bend side to side. The combination of these features allows slight displacements in the xy plane, as well as slight twists about the x and y axis. Additionally, the flat square shape at the bottom of the part is to provide a sturdy location for clamping into a vice while tapping the threads for the leadscrew. This feature is designed for manufacturing and does not serve a functional purpose in the performance of the part. A flaw in this design is that the original bolt pattern placed the threaded $\frac{1}{4}$ -20 mounting holes directly above the outer portions of the oval section. This prevented a tap from passing through the part sufficiently deep to form threads. Because of this, the bolt pattern was altered to place the mounting holes wider apart, past the ends of the oval. This allowed a tap to completely pass through the holes without interfering with the geometry below.

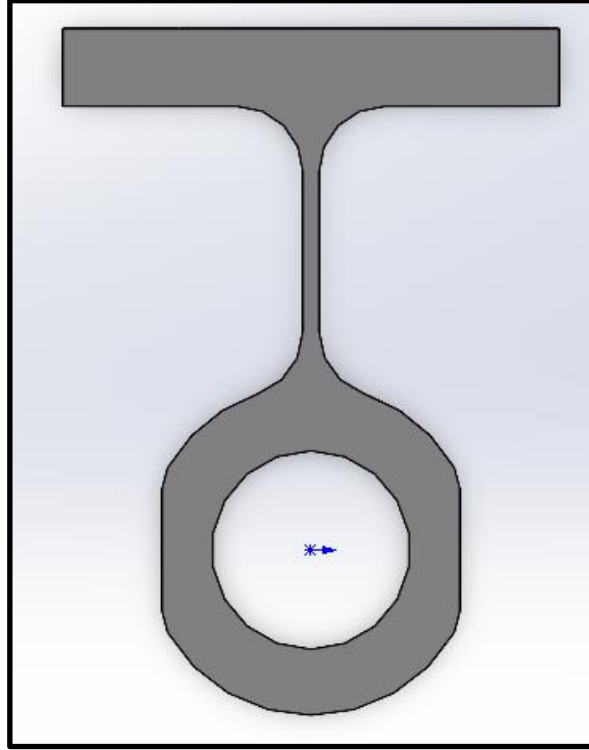


Figure 5: Guide Rod Flexure

The figure above shows the design of the guide rod flexure. This simple flexure accommodates imperfect parallelism between the linear guide rods. The single blade flexure allows for twisting about the y axis and displacement about the x axis. This flexure also has flat spots designed into the portion around the through hole. This allowed the part to be easily clamped in a vice while the hole dimension was finalized with a reamer.

2.2.2. Flexure Finite Element Analyses

To ensure that our flexures met the base requirements of our assembly, we put each flexure geometry through a set of simulations that would validate their fitness for our specific use case. A summary of our FEA parameters is featured in Table 1 and setup information for each FEA described in this section is included in Appendix B. Analysis was conducted mainly using ANSYS Mechanical and SolidWorks.

Table 1: Summary of FEA parameters and methods for testing.

Parameter	Criteria	Method
Strength	Stress (psi), Safety Factor	FEA with deflection and combined loading
Deflection Limits	Distance (in)	FEA with displacement loads
Resonance	2nd Base Frequency (Hz)	Modal analysis

Error	Distance (in)	FEA with combined loading
-------	---------------	---------------------------

To analyze these primary FEA parameters, each flexure was loaded with specific displacement values; these displacements are defined in Table 2. The cross-slide flexure is loaded laterally at a distance of 0.125” as a realistic maximum initial deflection as defined by the course instructor. The rail and lead screw flexures, meanwhile, are loaded angularly with edge displacements with allowance for deflection in their respective degrees of freedom. This loading was arbitrary, with the team defining a deflection of 0.01” as an incredibly conservative loading condition. Each flexure was subject to at least two simulations—basic loading conditions in either direction. Based on our error model, deflections as a result of alignment and loading will likely be 2 to 3 orders of magnitude lower; our analysis is therefore enveloping.

Table 2: Deflection values with resulting torsion.

Flexure	Deflection	Resulting Torsion
Cross Slide	0.125 in	N/A
Rail	0.01 in	~1.146 degrees
Lead Screw	0.01 in	~0.576 degrees (one axis) ~0.922 degrees (three axes)

Material and geometry choices were validated using stress analysis as related to yield strength and modal analysis. We defined the yield strength of Aluminum 7050 as 68000 psi as a conservative estimate based on the lowest grade of the material. We set a target safety factor of 1.5 as a measure of success. Modal analysis was conducted with respect to both the unloaded and loaded conditions for each flexure. The target frequency for the material was set at 20 Hz based on our machining speed parameter of 1200 rpm; a structure is successful if all relevant modal frequencies clear this base value. Results for both conditions are presented for each flexure in this section. Note that the results are largely in line with each other in terms of clearance above our target modal value. Results were analyzed using the 2nd lowest base resonant frequency as an accommodation for realistic loading conditions based on the advice of the class instructor. All joints are considered revolute, and for more realistic loading fixed supports are eschewed in favor of revolute joints to ground (assumed to be the carriage) for all three flexures.

Basic deflection analysis as a result of machining loads was also conducted for all three flexures for the sake of developing the HTM model. A more robust analysis would take into account full deformation effects as a result of machining forces and appropriate flexure preloads in the form of a heuristically-defined full-body analysis including the carriage geometry and utilizing revolute joints at interfaces with the rail assembly—we stop short of doing so in this paper.

The results for the deflection-based cross-slide analysis are shown in Figures 6 and 7. Maximum stress seen under a simple preloading of 0.125” deflection is ~7162 psi, yielding a safety factor of 9.5—a massive success with respect to target. Modal analysis also indicates a clearance above our 20 Hz threshold, with the second resonant frequencies being 108.39 Hz and 204.49 Hz for the unstressed and stressed conditions, respectively; first resonant frequencies also clear.

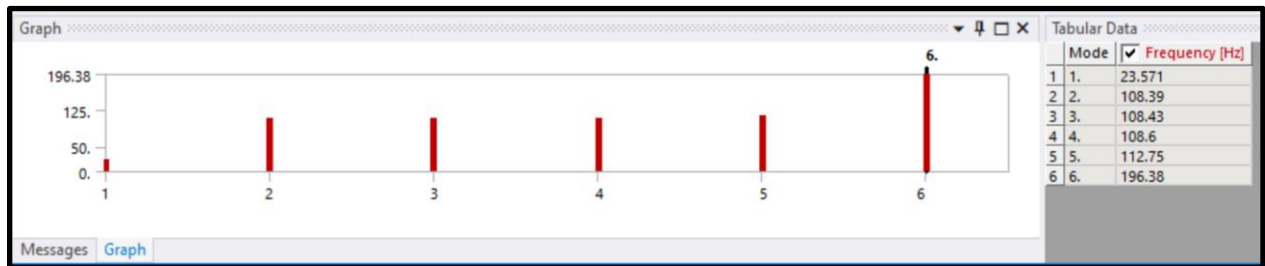


Figure 6: Modal analysis on cross-slide flexure with no initial loading.

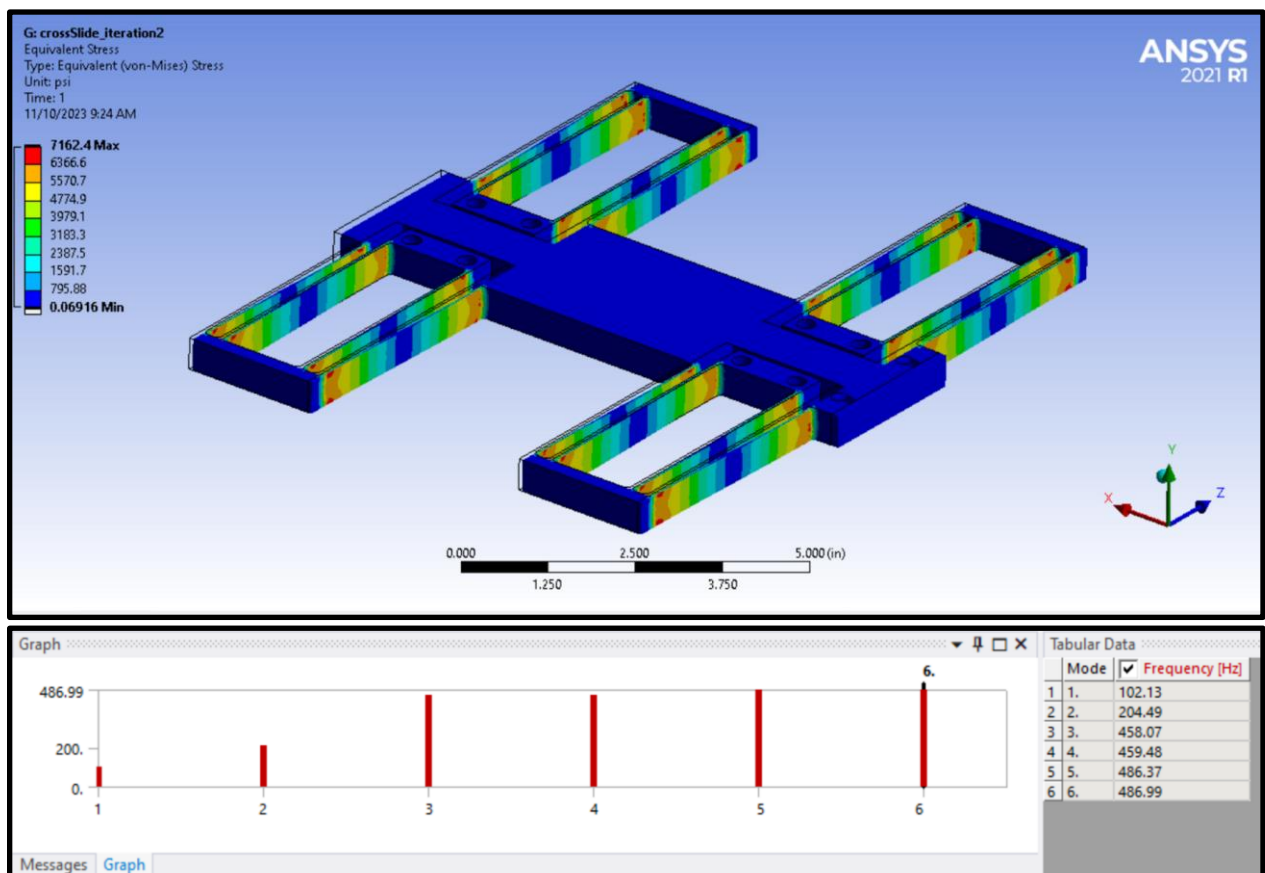


Figure 7: Stress (top) and stressed modal (bottom) analysis of cross-slide flexure.

Deflection analysis was also conducted on the cross-slide assembly with machining forces; the results of this analysis are shown in Figure __. Initial deflection was set at 0.125” maximum deflection, and the resulting maximum deflection is approximately the same in that direction. Therefore, it can be assumed that deflection as a result of machining forces is minimal.

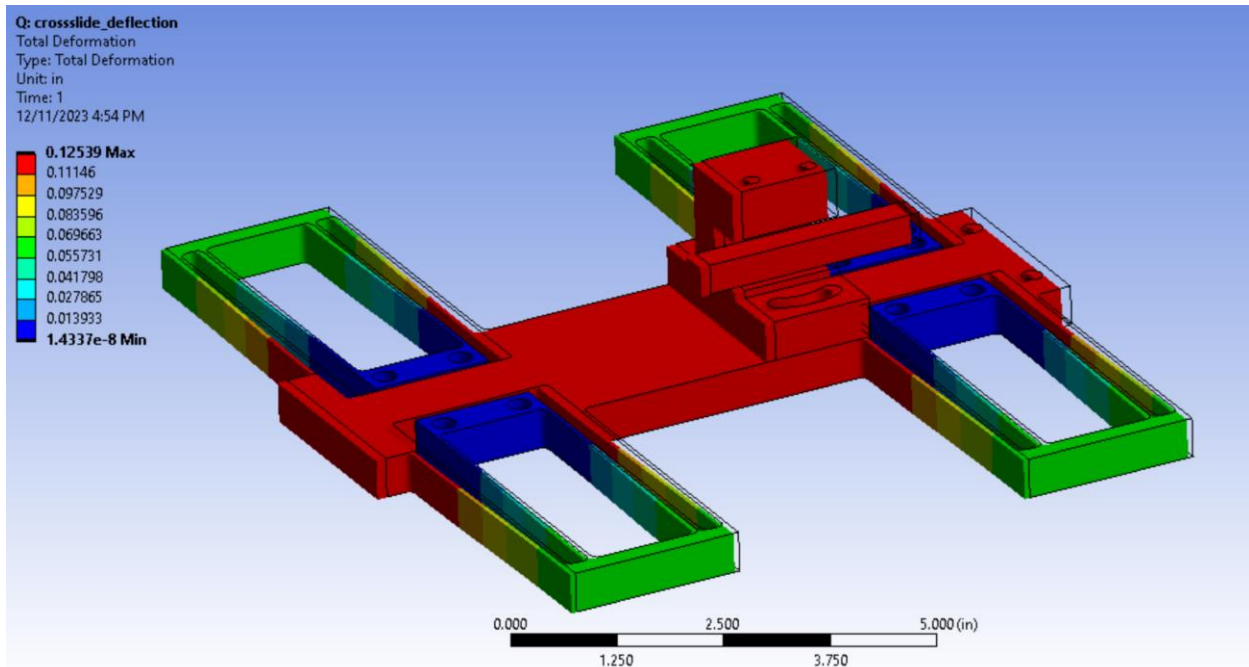


Figure __: Deflection of cross-slide structure under machining forces with initial 0.125” loading.

The rail flexure analysis featured in Figures 8 and 9 were conducted using the angular deflection showcased in Table 2. Loading in this simulation was applied at one edge of the central hole of the flexure; while not the most elegant loading case, it serves well to showcase torsional effects. Peak stresses seen are approximately 26000 psi, which yields a safety factor of 2.62, which clears our defined success threshold. Likewise, modal values are all above the 20 Hz threshold, with both second level frequencies being above 500 Hz and first level frequencies being above 150 Hz. The loading case highlighted in Figure 10—which propagates machining forces through the upper fixture—showcases minimal deflection as a result of machining; most deflection will be the result of errors in alignment of the rails.



Figure 8: Modal analysis on rail flexure with no initial loading.

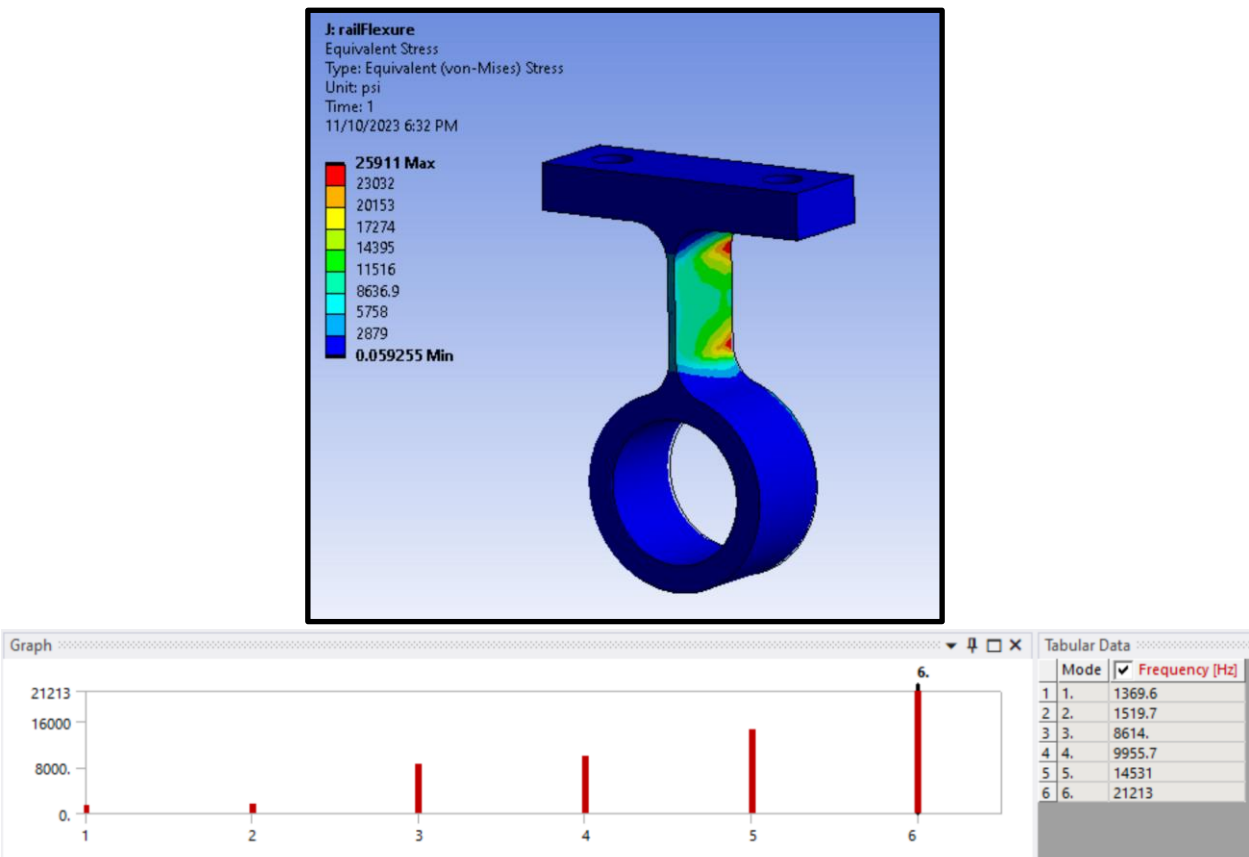


Figure 9: Stress (top) and stressed modal (bottom) analysis of rail flexure.

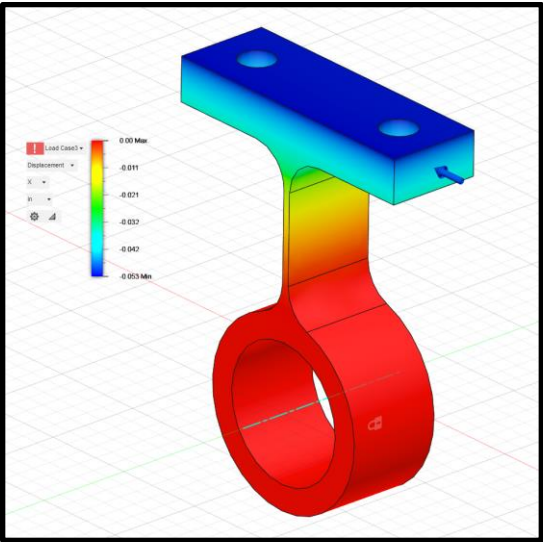


Figure 10: Guide rail flexure finite element analysis for lateral stiffness characterization.

The lead screw flexure is unique as it enables a degree of freedom in all three axes; therefore special considerations have to be taken in the setup of the analysis. Rather than simply two, eight simulations were run on this setup, with six serving as displacement in each axis in both directions (with torsional deflection of 0.576 degrees) and two serving as combined loading conditions (with torsional deflection of 0.922 degrees). Results of this analysis are shown in Figures 9, 10, and 11. The loading condition was similar to that of the rail flexure, with deflection conducted from the Disregarding the stress singularity at the displaced edge (a function of the loading condition), stresses overall are largely within margin, with an approximate peak of about ~27000 psi at the connection with the top fixture. With this assumption, this yields a safety factor of about 2.5, which passes our criteria. Modals all clear our 20 Hz threshold.



Figure __: Modal analysis on lead screw flexure with no initial loading.

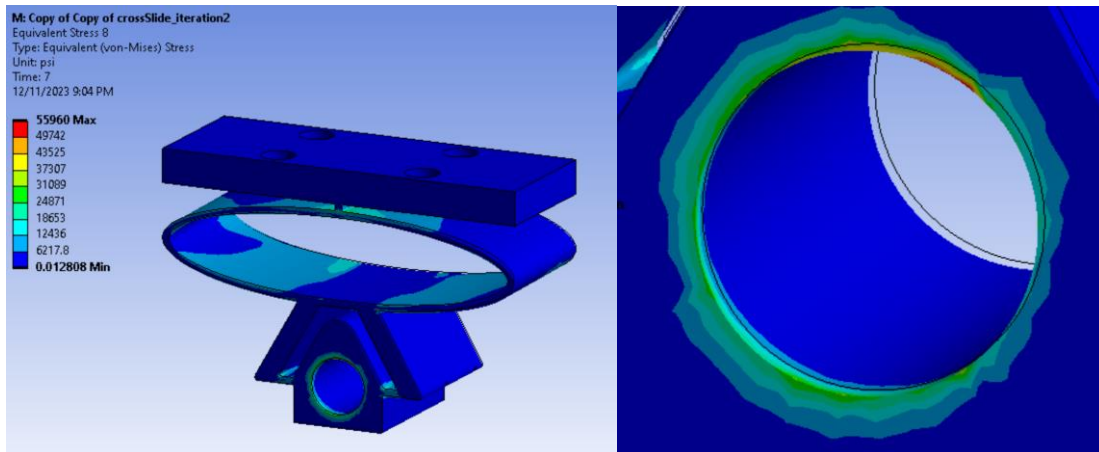


Figure 9: Maximum stress (left) condition of lead screw flexure with loading in 3 axes, alongside focus on infinite stress element (right) which resulted from loading definition on edge.



Figure __: Stressed modal analysis of lead screw flexure.

For deflection analysis and stiffness characterization, two machining-force-centered loading conditions were defined in the lateral and vertical directions; results are shown in Figures __ and __ below. Both loading conditions result in minimal deflection, maintaining the trend seen with the other two analyses.

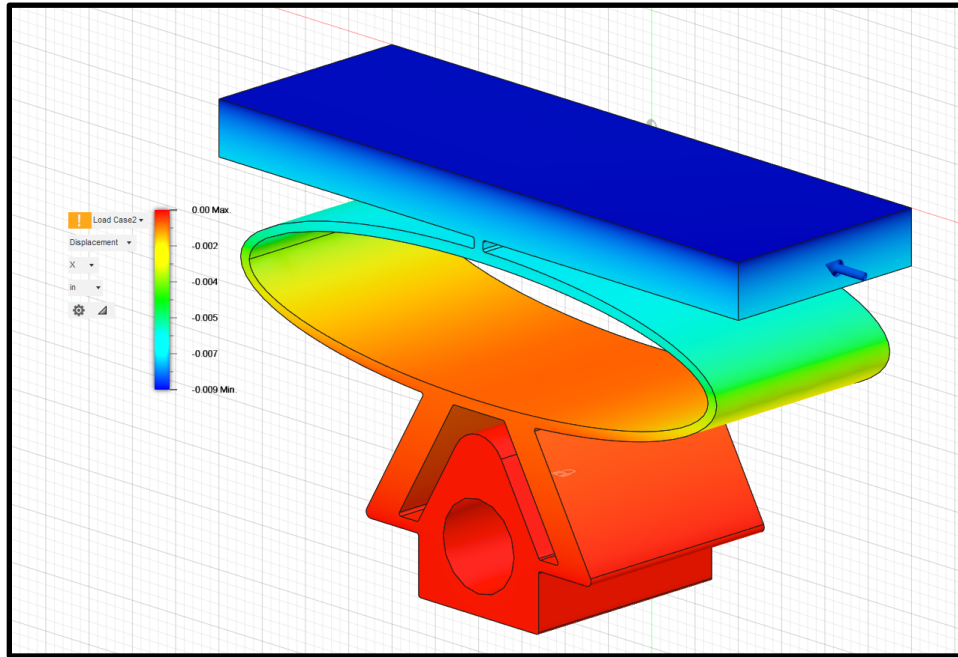


Figure 11: Leadscrew flexure finite element analysis for lateral stiffness characterization.

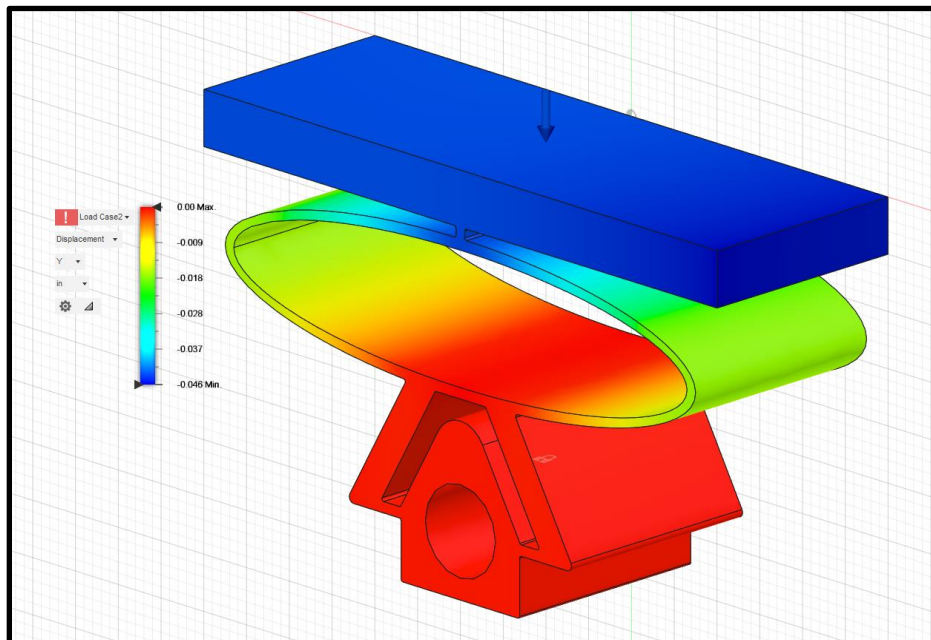


Figure 12: Leadscrew flexure finite element analysis for vertical stiffness characterization.

2.3. Belt and Pulleys

2.3.1. Belt and Pulleys Selection

From the cutting force calculations, an ideal angular velocity that suits the feed velocity of 600 ft/min is 2291.8 rpm. However, the motor is only 0.5 horsepower which will decrease this desired angular velocity. With these requirements, the pulleys and belts were initially selected through intuition but then verified to work with calculations. The team selected a 2.5" pulley for the spindle and a 4.95" pulley for the motor. These pulleys were chosen as the closest match to a 2:1 ratio, while having the correct keyway dimensions and shaft size to mate with the other parts in the system. The 2:1 ratio was selected to achieve the maximum desired cutting speed at the motor's maximum load RPM. A 33" v-belt was selected to connect these two pulleys together. This allowed the motor to be mounted far enough from the rest of the lathe to adequately clear all of the other components. From these initial conditions, the center-to-center distance, Appendix C, was 10.918". The initial tension needed to be 9.986 lbf. An issue that could occur though with this system is that the fatigue safety factor is 0.7827. This is low but the time this system will run for is a maximum of 1 hour, which negates any fatigue failure. If we wanted to create a long-lasting system, then 2 belts would be needed.

2.3.2. Belt and Pulleys Model

Figure 12 below shows the 3D CAD model of the motor and lathe assembly. The black part in this virtual environment is the motor, the brown part is the wooden mounting platform, and the multicolored silver part is the lathe. The mounting platform is 20" by 30" and consists of a 6 mm laser-cut plywood sheet secured to a 15mm particle sheet. The motor and lathe are connected to each other via a belt and pulleys system. The center-to-center distance between the two pulleys is 11" which is rounded from the length calculated in Appendix C. To secure the head and foot caps and the motor to the mounting platform, 5/16" - 24 bolts were used. The motor was tightened using nuts while the caps were tapped.

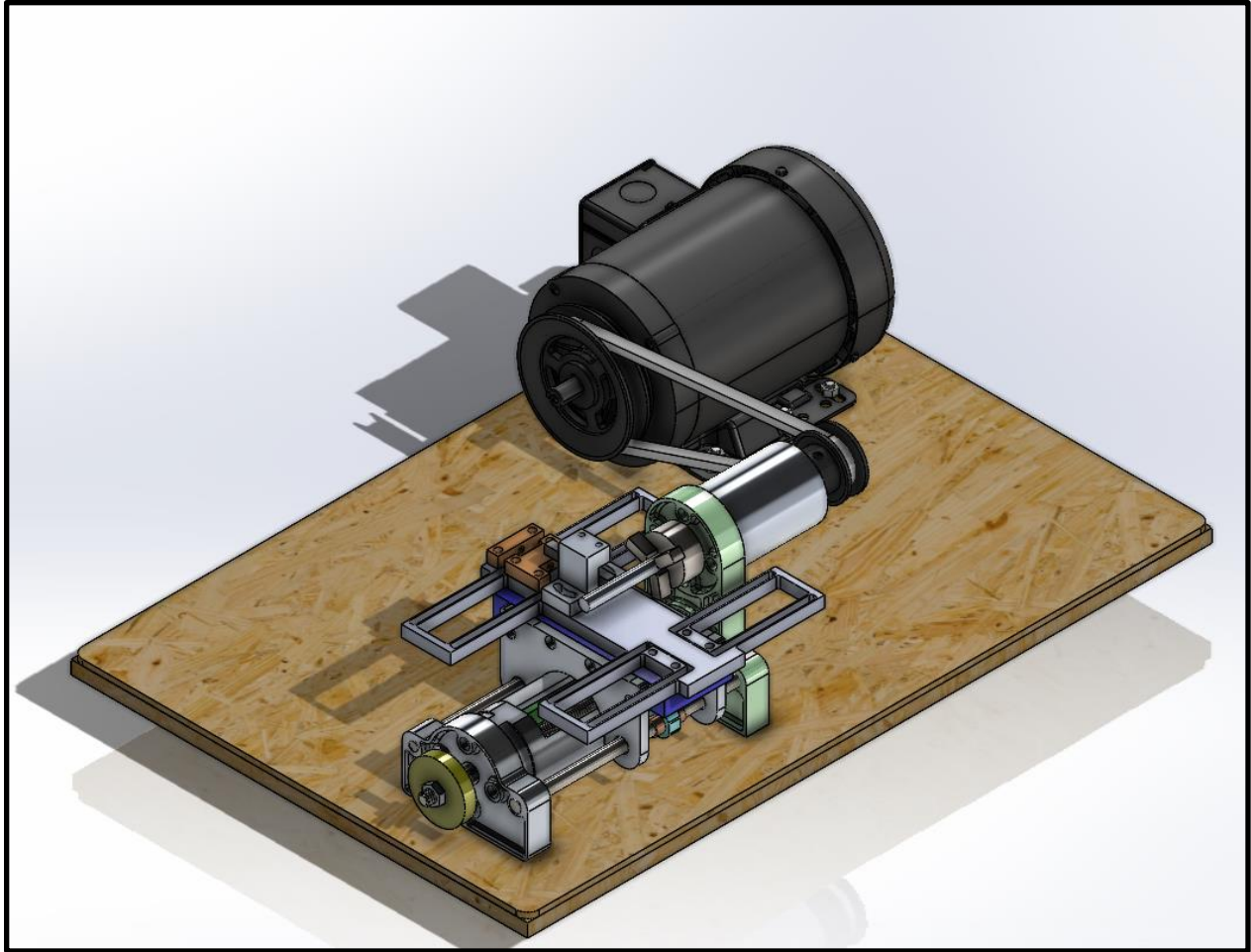


Figure 13. Isometric view of the motor and lathe on the mounting platform.

Figure 13 below shows the front view of the belt and pulleys system. In this image, it is clearly seen that the larger pulley on the motor is below the smaller one on the lathe. The center-to-center distance is not disrupted in this situation which allows a distance of 11" to be suitable.

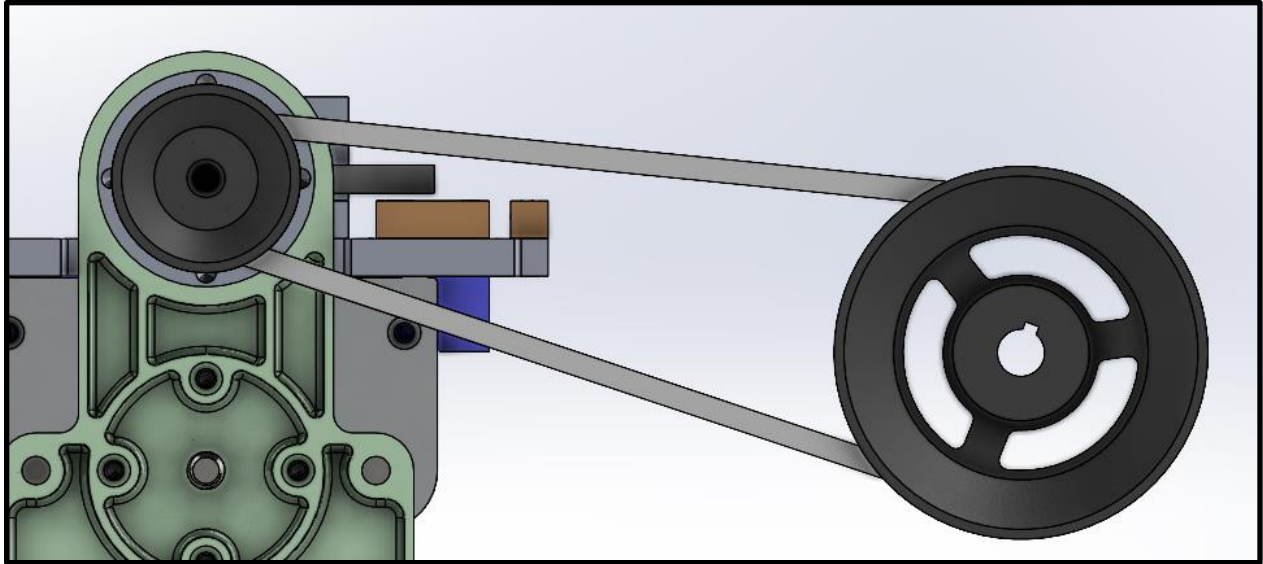


Figure 14. Front view of belt and pulleys.

2.3.3. Belt and Pulleys Assembly

Figure 15 below shows an image of the physical motor and part of the lathe on the mounting platform. The mounting holes for the motor were slotted to allow for belt tension adjustment. The motor was first installed loosely, then the belt was slipped over both pulleys, then the motor was pulled away from the lathe to provide initial belt tension while the motor mounting bolts were tightened into place. Here the belt is also seen with a satisfactory tightness around the pulleys. The two sheets of wood are fastened together with 1.5” wood screws.

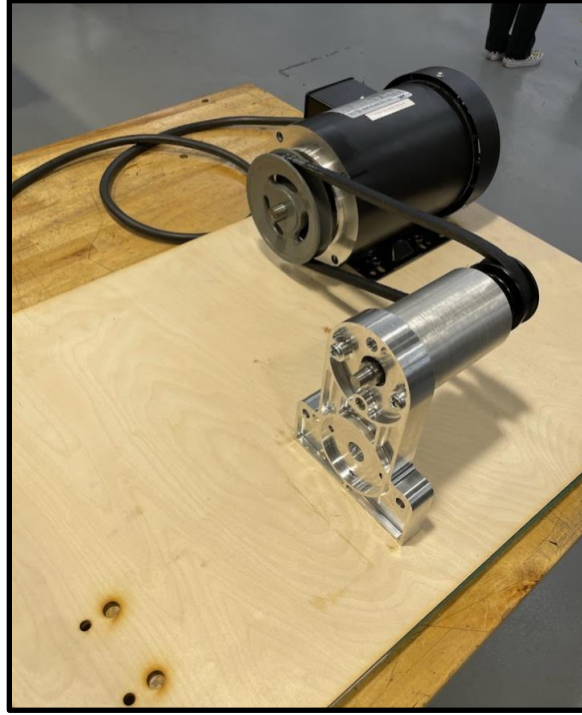


Figure 15: Isometric view of the physical motor and head cap on the mounting platform.

3. Manufacturing

For the manufacturing of this project we followed a general procedure for all the components we had to machine, the spindle, the dial holders, and the shaft. What we did followed a three-step plan. First, we prepared the stock material by cutting them to length or by turning them to the final diameter depending on the corresponding material. Then we performed the main machining procedure on each, for the spindle and shaft we used the lathe, and for everything else we used the mill to be able to manufacture everything to their final design. Once everything was done we performed simple clean-up techniques from filing corners and sanding faces.

Fabrication of the parts of the lathe required the use of several advanced machining techniques. This included boring bars for machining deep IDs inside blind holes, radius tools for cutting filets into stepped corners, and precise manual tapping of exotic thread forms. Machining drawings were created before beginning many of the complex parts to reduce the chance of errors being made and to provide a useful reference during the machine tool operation.

4. Error Model

A model for the error of the lathe was created to characterize the accuracy under expected operating conditions. The set of operating conditions chosen for the analysis consists of expected cutting forces and location.

The model is divided into two “loops”, the spindle loop and the tool loop, with each loop beginning at the tool-part interface and terminating at the ground. In this case, the ground is at the bottom of the headstock. The loops are networks of nodes and links, with nodes placed in locations along each loop with relative motion due to member stiffness. The loop geometry is defined by a set of homogeneous transformation matrices (HTMs) for each set of nodes.

4.1. Spindle Loop

The spindle loop can be seen in Figure 16 below.

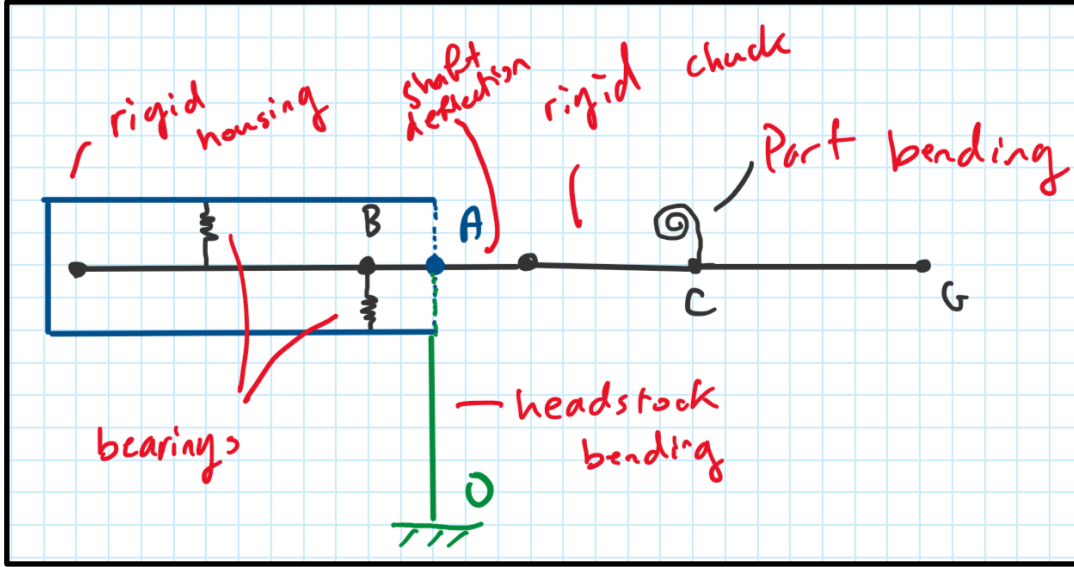


Figure 16: Visual representation of spindle loop.

It consists of 5 nodes, including ground.

- Node G is located at the part-tool interface and is the node used to define the expected accuracy of the machine.
- Node C is located at the base of the part to be machined, with the link CG being the part.
- Node B is located at the proximal bearing, relative to the headstock. Link BC is part of the spindle shaft as well as the chuck.
- Node A is located at the centerline of the upper bore of the headstock, coinciding with the shaft centerline. Link AB is a parallel set of links that include the spindle housing.
- Node O is located at the ground. Link OA represents the headstock.

The relative locations of the nodes are defined by the design’s geometry. The error, therefore, can be described by the locations before and after loading. The formulation is as follows

$$H_G^O = H_A^O \cdot H_B^A \cdot H_C^B \cdot H_G^C \quad (1)$$

$$error = (H_G^O)_{loaded} - (H_G^O)_{unloaded} \quad (2)$$

For link CG, the deflection of the part is described by bending along two axes due to the cutting and thrust forces. It is modeled as a cantilever beam, with a fixed support at the chuck. The chuck is assumed to be rigid, therefore, transmitting loads down the shaft with no relative deformation. A simple visual representation is shown below in Figure 17. The deflection at G can be calculated using a standard formulation for a cantilever beam in bending.

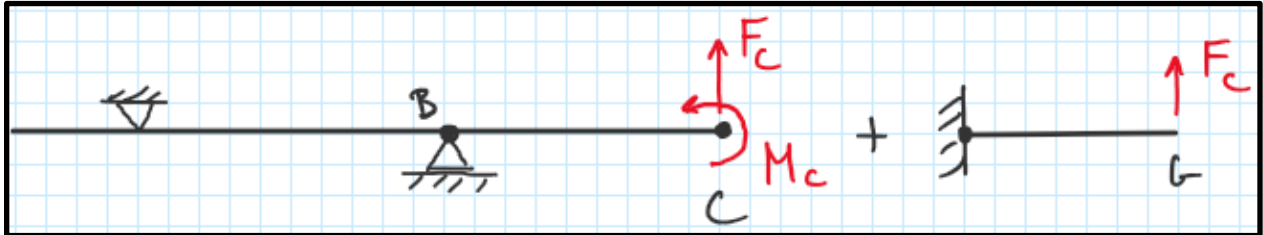


Figure 17: Visualization of part and shaft bending along one axis.

Also shown in Figure 17 is the spindle shaft bending due to the cutting force and moment, with the same representation applying to the thrust force and moment. The shaft is considered to be fixed at the bearings, with the motion of the bearings being characterized in a different link. Finite element analysis was used to characterize the deflection at the jaws of the chuck, node C.

To describe the rotation of the spindle (orientation of a reference frame placed at node B), a rigid part, chuck, and shaft are used, resulting in an angle of rotation only due to bearing deformation. Bearing deformation is dependent on stiffness and loading (reaction forces).

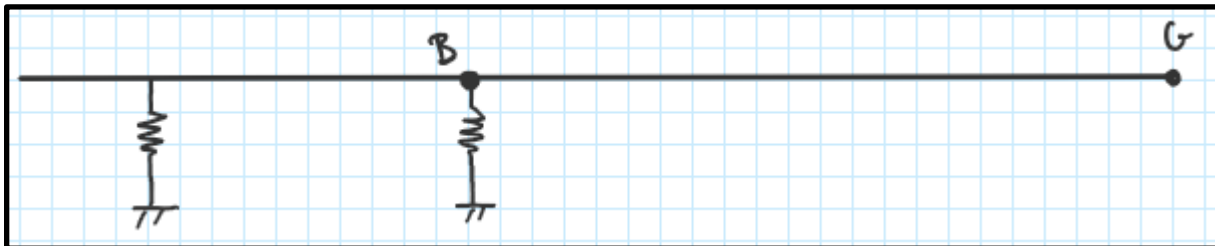


Figure 18: Rotational stiffness due to bearings model.

The bearings, included in link AB, are attached to the headstock through the housing, and therefore, experience rotation and translation due to the headstock deflection. A visual representation is shown below.

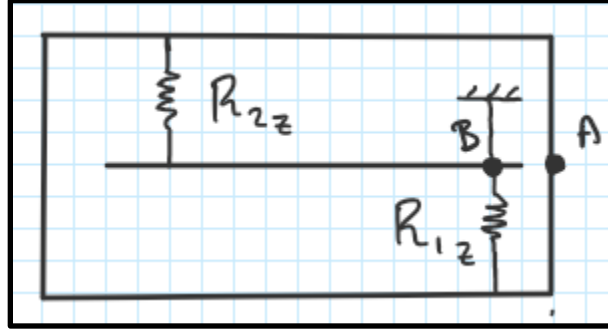


Figure 19: Link AB.

Finally, the bending of the headstock (Link OA) due to cutting and thrust forces and moments, is calculated using FEA.

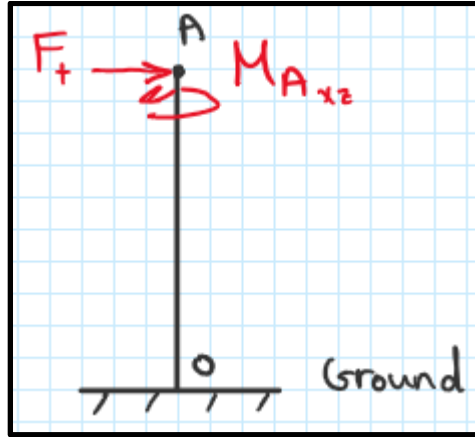


Figure 20: Headstock loading.

The results from the model yield the following error at the part-tool interface.

$$\delta_x = -0.002 \text{ in}, \delta_y = 0.001 \text{ in}, \delta_z = 0.0022 \text{ in}$$

The x-axis is along the centerline of the spindle shaft and part, the z-axis is the vertical axis of the lathe (along the height of the headstock), and the y axis is normal to both x and z and is the thrust direction.

4.2. Tool Loop

The tool side loop of the error model can be seen in Figure 21 below.

It consists of 4 nodes, including ground. Nodes G and O are shared across the two loops.

- Node I is located at the first fixed point along the tool with the link IG being a section of the tool under bending.

- Node J is located at the bottom of the carriage. Link JI includes a parallel set of links that represent the upper leadscrew and cross-slide flexure.
- The network of links OJ includes the leadscrew flexure, the guide rod flexure, and the guide rods. It is a parallel set of links, along each link is a varying set of stiffnesses due to the components along the links.

The error at the part-tool interface through this loop is formulated as:

$$H_G^O = H_J^O \cdot H_I^J \cdot H_G^I \quad (3)$$

$$error = (H_G^O)_{loaded} - (H_G^O)_{unloaded} \quad (4)$$

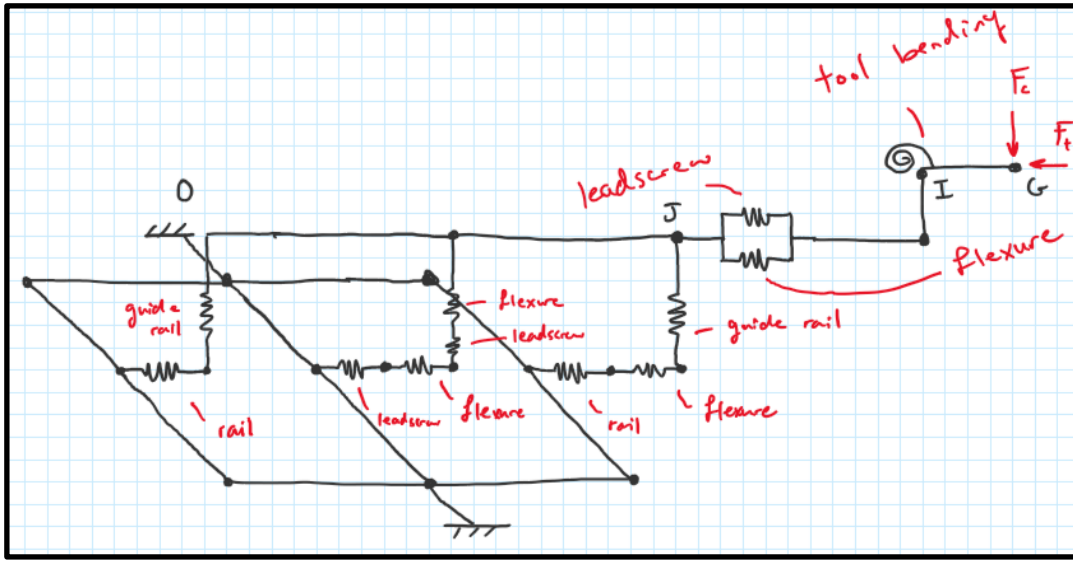


Figure 21. Visual representation of tool side loop.

The tool (link IG) is modeled as a cantilever beam in bending, solely due to the cutting force. The deflection at the tip of the tool can be calculated using the standard formulation used for the part deflection calculation.

For link IG, the stiffnesses of the two members along the network are required to determine the load split between them along the thrust direction. The expectation was that the lead screw is much stiffer than the flexure, and therefore, most of the load would travel through it. The following values were obtained for the stiffnesses

$$k_{lead screw} = 1.394 \times 10^6 \frac{lb_f}{in}, k_{flexure} = 58.57 \frac{lb_f}{in}$$

As expected, the link stiffness is dominated by the leadscrew, and therefore, the flexure experiences little to no loading in the thrust direction. As a result, the relative motion, due to thrust,

of node I with respect to node J is determined by the deformation of the lead screw, which is in compression. A standard beam in the compression model is used to calculate the deformation of the parallel set of links.

For the link network OJ, the stiffness along three axes is analyzed, which are the cutting and thrust directions, as well as the rotational stiffness about the feed axis (normal to the cutting and thrust). The network along the cutting axis is shown below.

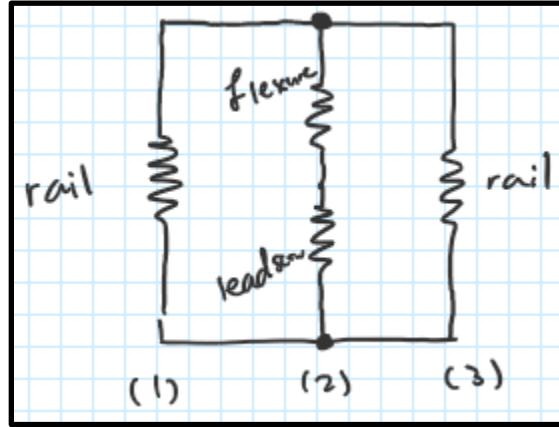


Figure 22. Network OJ along the cutting axis.

The leadscrew flexure and leadscrew are in series, and together they are in parallel with the two guide rails. To calculate the load split along the three branches, the stiffness of each branch must be calculated. It is expected that the guide rod branches are much stiffer than the flexure branch due to the flexure stiffness being in series with the lead screws. The stiffness values were calculated and are shown below.

$$k_{rail} = 2.144 \times 10^4 \frac{lb_f}{in}, k_{flexure} = 597.8 \frac{lb_f}{in}, k_{leadscrew} = 1.12 \times 10^4 \frac{lb_f}{in}$$

$$k_2 = 567.5 \frac{lb_f}{in}$$

According to the calculated stiffness values, approximately 1.3% of the cutting load is transmitted through the flexure-leadscrew branch, while the remaining load is split evenly between the two guide rail branches. This means the deflection of node J relative to node O in the cutting direction is primarily dependent on the guide rod deflection due to bending. The guide rod deflection is calculated using a beam with a two fixed supports model.

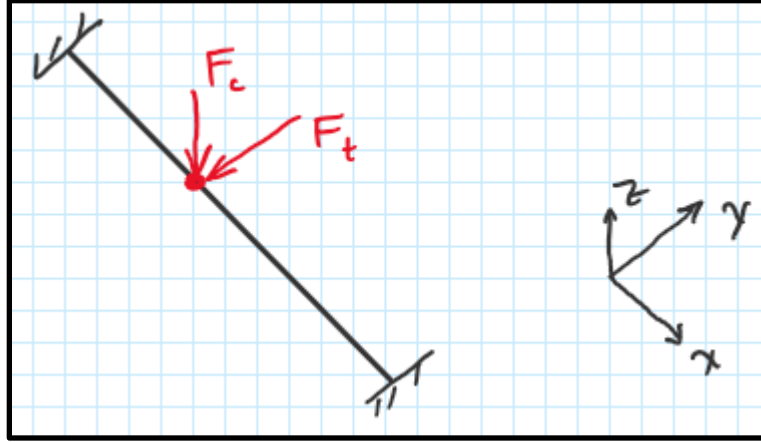


Figure 23. Guide rod model.

The same procedure is applied for the thrust direction, and is shown below.

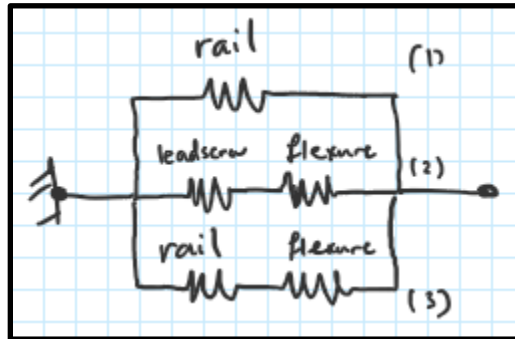


Figure 24. Network OJ along the thrust axis.

The stiffness of the guide rod flexure in the thrust direction results in split of loading that is primarily dominated by the sole rail stiffness branch. The stiffness values and member loading bearing percentages are shown below.

$$k_{rail} = 2.144 \times 10^4 \frac{\text{lb}f}{\text{in}}, k_2 = 741.44 \frac{\text{lb}f}{\text{in}}, k_{leadscrew} = 134 \frac{\text{lb}f}{\text{in}}$$

$$C_1 = 96.1\%, C_2 = 3.32\%, C_3 = 0.6\%$$

Due to the flexure stiffness being 2-3 magnitudes lower than the guide rod, the guide rod bears 96.1% of the thrust load.

Finally, the rotational stiffness of the network OJ is modeled as follows.

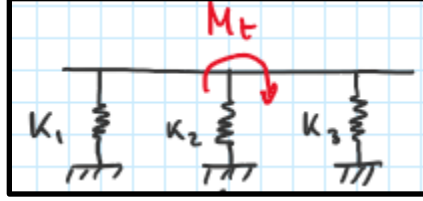


Figure 25. Rotational stiffness of network OJ due to stiffness couples.

The stiffness couples result in a rotational stiffness about the normal axis. As a result, the deflection of the stiffest branch(s) determines the overall rotation of the reference frame present at node J. The leadscrew and guide rail flexures have much lower rotational stiffness in this direction. Therefore, the rotation is primarily dependent on the couple stiffness.

The resulting error at the tool-part interface is

$$\delta_x = 0 \text{ in}, \delta_y = -0.0001 \text{ in}, \delta_z = -0.00045 \text{ in}$$

The final error at the point of machining along all three axes can be seen in the following table. These results indicate that the tool side of the system has a higher stiffness than the spindle side due to the smaller errors calculated.

Spindle Side Error (in)	$\delta_x = -0.002$	$\delta_y = 0.001$	$\delta_z = 0.0022$
Tool Side Error (in)	$\delta_x = 0$	$\delta_y = -0.0001$	$\delta_z = -0.00045$

5. Metrology

In order to characterize our lathe and measure its accuracy, repeatability, and the overall error present in our system, we utilized some metrology approaches. Namely, we conducted spindle runout testing to measure the error present in our spindle assembly during rotation, as described below.

5.1. Spindle Runout

Spindle runout testing is a method for measuring the runout error of the spindle assembly by setting up the spindle with a test cylindrical sample, rotating the spindle to set degrees, and measuring the distance to the sample from the sensor. By averaging the results of two of these tests, with the spindle rotated 180° degrees between tests, and plotting the radial results as a function of degrees on a polar graph, we can visualize the spindle rotation and observe whether or not the spindle assembly is performing the way we want - i.e. whether or not there is error in its movement.

Our team had to conduct spindle runout measurements multiple times for a number of reasons related to the test setup and the quality of our spindle assembly. During our first test we encountered issues with reaching the sensors maximum/minimum values. Because our sensor wasn't setup/calibrated properly, during testing the output would reach the maximum (or minimum) point and the subsequent measurements were inaccurate. During our second test our measurements were inconsistent because of two distinct issues with our spindle assembly. First and foremost, our assembly utilized two nuts back to back - this was done to prevent the preload nut from loosening and twisting off of the spindle during use. The second nut was used to keep the first in place. However, during the runout measurements we noticed that when the nuts were kept loose enough to rotate the spindle by hand, the runout measurements were inconsistent - the first and last data points were significantly different, even though they were taken at the same location, pointing to the fact that the spindle was loose. On the other hand, when both nuts were fully tightened (hand tight), the spindle could not be rotated by hand. This led to difficulty in properly calibrating the sensor and runout measurements that displayed significant error. Furthermore, when testing with both nuts tightened, we noticed significant grinding sounds in our spindle assembly.

Because of the result of the second test, we had to take apart the spindle to determine the source of the grinding sound, as it was likely the cause of the spindle over tightening and the runout measurements having a lot of error. When the spindle assembly was taken apart we noticed that the step in the housing that was used to space the two bearings apart was larger than the outer race of the bearings, as seen in Figure 26 below. This led to the inner race making contact with the step and rubbing against it during spindle rotation. Although the step diameter was sized to accommodate the spindle passing through it, it was not considered that the inner race would protrude past the outer race on the side where the step is when fully installed. This prevented the inner race from fully seating in the outer race, causing the initial runout measurements to be erratic. This introduced additional friction when the preload nuts were tightened and caused damage to both the housing and the bearings. The issue was corrected by using a boring bar to increase the ID of the stepped section to sufficiently clear the inner race. This only required a small amount of material to be removed near the face of the step.

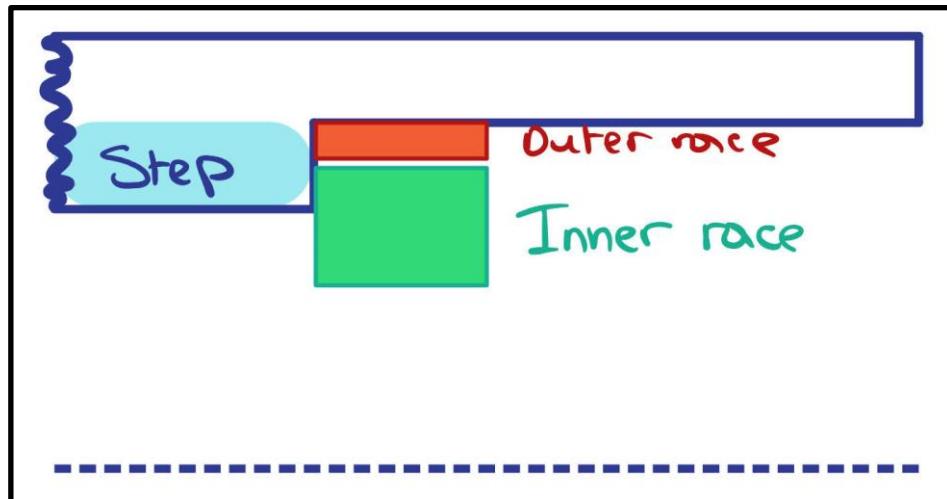


Figure 26. Interference of the Housing Step and the Bearing Inner Race.

After the housing step was machined to reduce its size down to the diameter of the outer race of the bearings, runout measurements were taken again. Appendix C contains the obtained data as well as the code used to conduct the runout calculations and plot a visual representation of the spindle runout error. The resultant plot can be seen in Figure 26 below.

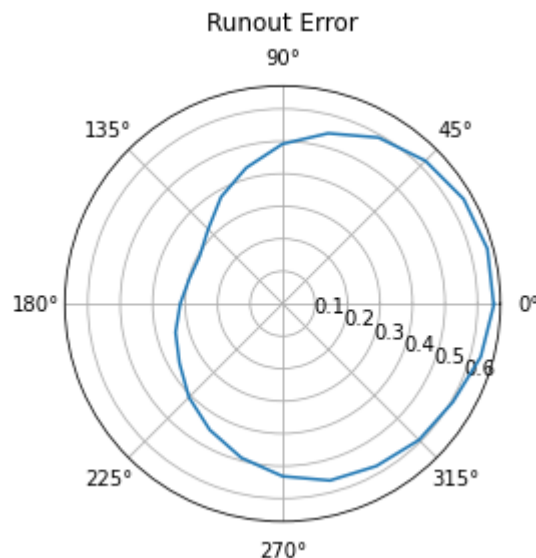


Figure 27. Spindle Runout Error

As can be seen in the figure above, our spindle assembly unfortunately displays a significant amount of error. With a visualization factor of 50, our plot displays the largest difference in radius as being approximately 0.37, from a maximum point of around 0.67 (0.17 above the base 0.5 in radius) to a minimum point of around 0.3 (about 0.2 below the base radius). Furthermore, we can infer the accuracy of our spindle rotation from the symmetry of the plot above. Again, the plot is highly asymmetrical, with one side of the plot having a much larger radius than the other.

Overall, the results of our experiment show that our spindle assembly is not as accurate as it should be, and in the future changes should be made to increase accuracy. Mainly, more care must be taken during machining to improve the dimensional accuracy of our components as well as decrease the number of imperfections.

6. Performance

During the cutting test the team observed a number of issues with our lathe, which resulted in less-than-ideal performance. The main issues were: incorrect design and assembly of the leadscrew subsection of the lathe, inability to raise and lower the cutting tool, and nonideal performance of the spindle assembly that was covered in the previous section.

The final assembly of the lathe revealed that our lead screw assembly wasn't fully operable. Namely, our team struggled with making the leadscrew engage with the stage to move it forward and back rather than twisting the leadscrew itself forward or back through the assembly. We discovered that the leadscrew was capable of engaging, however, it had a very large amount of backlash involved that resulted in the leadscrew backing up a significant amount through the assembly before engaging when we would change directions. This meant that the leadscrew came very close to coming out of the assembly, which would mean that the entire leadscrew housing would have to be taken apart in order to reconnect the internal nuts, washers, etc.. Furthermore, when the leadscrew was engaged and moving the stage during the cutting test, the amount of torque required to rotate the leadscrew was very large, resulting in the inability of our team to continuously move the stage forward by hand strength alone.

Though it is impossible to say exactly what was wrong with the leadscrew assembly without taking it apart, our team can make an informed guess regarding what caused the issues we observed. First and foremost, as discussed in section 4.1, our spindle assembly had issues with internal friction due to incorrect part dimensioning which led to our inability to turn the spindle by hand. It is hypothesized that a similar issue is at play in the leadscrew assembly. Due to the high input torque required to turn it, we can assume that some parts of the leadscrew assembly were producing unaccounted-for friction. However, we would have to disassemble the leadscrew housing to observe which areas could have had interference or, as in the case of the spindle assembly, look for damage and debris that resulted from the interference in order to determine where it took place. Next, in the case of the massive backlash, we have a substantial theory stemming from concerns during assembly. When we were assembling the leadscrew subsection we noted that the nuts on either side of the leadscrew that preloaded the bearings (alongside with the spring washers) and kept the bearings in place were not supported on both sides - the side not facing the bearing had a gap between the nut and the cover plate. We believe that during operation the tightened nuts would loosen due to that gap, with no way to tighten again until they reached the opposite side of the gap,

causing backlash in our system. This theory is further supported by the fact that when turning the leadscrew by hand after assembly we could feel the nuts come loose, but due to the fact that the cover plates were press fit to the cylinder in such a way that they were almost impossible to separate without damaging the components we were unable to address this issue prior to the cutting test. Both of these issues have to be fixed in order to allow for smooth functionality of the lathe. While the lathe was able to cut as is, caution had to be taken to ensure the leadscrew did not back out of place. The excessive backlash caused a very significant slowdown during direction changes between passes, and the excessive leadscrew friction limited the feed rate at which the operator could drive the leadscrew. These were the limiting factors that reduced the overall cut speed.

Another issue that our team encountered during the cutting test was the inability to raise or lower our cutting tool. Unfortunately, this capability was not designed in our lathe, resulting in us not being able to place the cutting tool at the proper height to be able to cut correctly. We were able to address this issue during the testing by placing the cutting tool upside down (thus lowering the sharp edge of the tool to the correct height) and setting our motor in reverse to cut in the opposite orientation from the standard. This allowed us to cut our cylindrical sample during testing, however, the ability to raise and lower the cutting tool must be added for the proper functionality of our lathe.

7. Conclusion

As discussed in section 5 above, our team encountered a number of challenges during the cutting test. Though we were able to obtain a successful cut using our machine, a number of improvements need to be made to optimize the functionality of our lathe.

7.1. Improvements

Though continuous improvement is possible in any machine, including our lathe, there is a number of required changes that must be implemented to allow for correct functionality of our machine. Those changes include improving the manufacturing of the spindle and housing to reduce the runout error, disassembling the leadscrew assembly to locate and identify the source of the internal friction so that it can be fixed, adding spacers into the leadscrew assembly to properly support the nuts and prevent backlash, and adding a method for raising and lowering the cutting tool.

First up, the machining processes conducted to manufacture the spindle, housing, and additional components of the spindle assembly need to be improved in order to reduce our runout error. Specifically, the spindle needs to be machined with a higher degree of accuracy to ensure concentricity of the spindle. Taking the time to improve the accuracy of our cuts and reduce any defects in our manufactured components could significantly improve the accuracy and repeatability of our spindle motion.

Next, in order to determine the true reasoning behind the high torque requirements and the excessive backlash of the leadscrew assembly, that subsection of our lathe must be disassembled and analyzed. Upon disassembly we can take the time to locate the errors/defects in our system so that we can determine the best way to correct them.

In the case of the leadscrew backlash, as discussed in the performance section of this report, our team already has a good idea of the reasoning behind the loosening of the nuts and the resultant backlash. Machining new spacers, utilizing a number of washers in place of spacers, reducing the length of the cylinder and its spacers to remove the gap between the nut and the cover plates are all possible approaches we could take to address this issue. However, until the leadscrew subsection of our lathe is disassembled, the damage is assessed, and the other sources of error and internal friction are found, we cannot make any other improvements to this assembly.

Finally, similarly to the leadscrew backlash solutions above, there are many different ways to design a system for raising and lowering the cutting tool. The easiest solution to our issue involves reducing the height of the tool holder to lower the minimum height of the tool, since the holder was simply too tall to begin with, resulting in us having no way to lower the tool, only raise it. Then, by utilizing the set screws and spacers/washers, the desired height of the tool can be achieved.

Overall, though our lathe was capable of producing a successful cut, there are a number of improvements we would like to implement to increase our accuracy and our chances of success. Given more time to make updates to our design, our team is confident that we could produce a much more successful tabletop lathe.

Appendix A

Cutting Force: $u_s = 0.15 \rightarrow 0.4$

$$\Omega = \frac{v_s}{\pi D} = \frac{600 \text{ ft/min}}{\pi \left(\frac{1}{12}\right)(1)} = 2291.83 \text{ rpm}$$

$$\begin{aligned} f &= \frac{v_w}{N \Omega} \rightarrow v_w = f N \Omega \\ &= 0.004(1)(2291.8) \\ &= 9.1673 \text{ in/min} \end{aligned}$$

$$\begin{aligned} MRR &= v_w \cdot \pi D \cdot d = 9.1673 \cdot \pi \cdot (1)(0.1) \\ &= 2.88 \end{aligned}$$

$$P = u_s MRR = 0.4(2.88) = 1.1520$$

$$\begin{aligned} F_c &= u_s f d = 0.4(9.1673)(0.1) \\ &= 0.366 \text{ lbs} \end{aligned}$$

$$\beta = \tan^{-1}(u) = \tan^{-1}(0.5) = 26.5651^\circ$$

$$F_T = F_c \tan(\beta - \alpha) = 5$$

$$\alpha = 25^\circ$$

Figure A.1. Cutting force calculations.

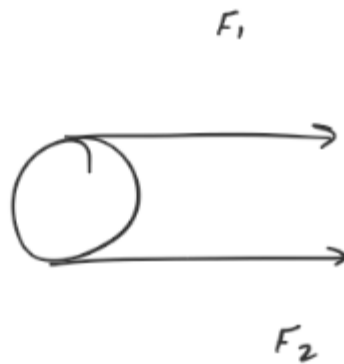
Pulley

$$r_c = \frac{d_c}{2} = \frac{1}{2} \text{ in}$$

$$T_c = F_c(r_c) = 63(1/2) = 31.5 \text{ lb-in}$$

$$T_c = T_p$$

$$T_p = F_p r_p = T_c$$



$$F_1 - F_2 = \frac{2T}{d}$$

$$d_y = 0.5$$

$$F_1 = F_2 \left(\frac{2T_c}{d_y} \right)$$

$$P = \frac{(F_1 - F_2)(\gamma)}{33,000}$$

$$\frac{33,000 P}{V} = F_1 - F_2$$

$$F_2 = F_1 - \frac{33,000 P}{V}$$

$$F_1 = \left(F_1 - \frac{33,000 P}{V} \right) \left(\frac{2(T_c)}{d_4} \right)$$

$$F_1 = \frac{2T_c}{d_4} F_1 - \frac{2 \cdot 33,000 \cdot P \cdot T_c}{d_4 V}$$

$$\frac{66,000 P T_c}{d_4 V} = F_1$$

$$\left(\frac{2T_c}{d_4} - 1 \right)$$

$$\frac{66,000 P T_c}{2T_c V - d_4 V} = F_1$$

$$F_2 = F_1 - \frac{33,000 P}{V}$$

$$T_{T1} = F_1 + F_2$$

Figure A.2. Pulley tensions calculations.

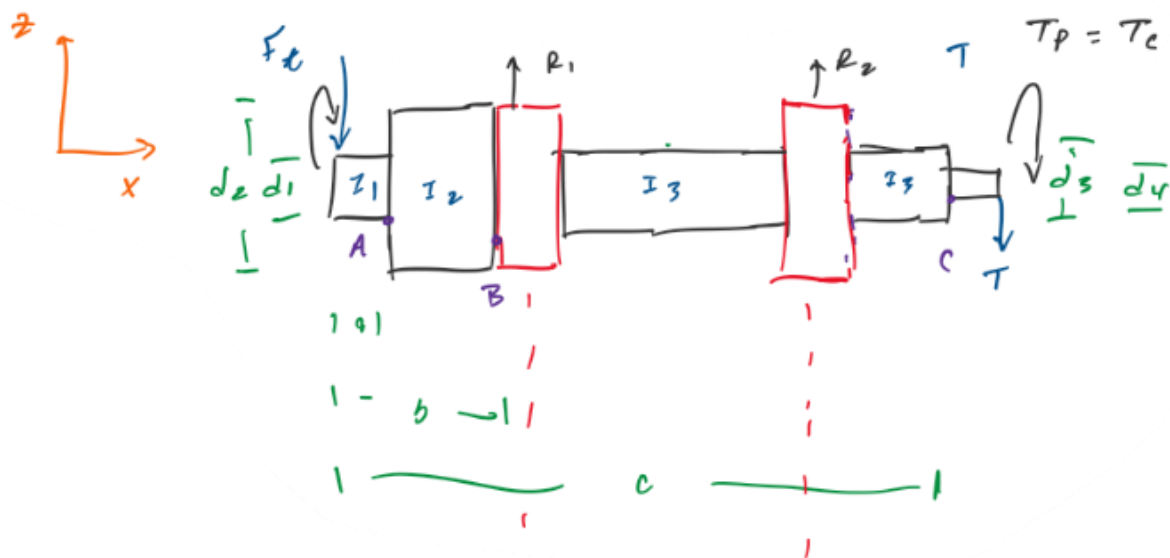
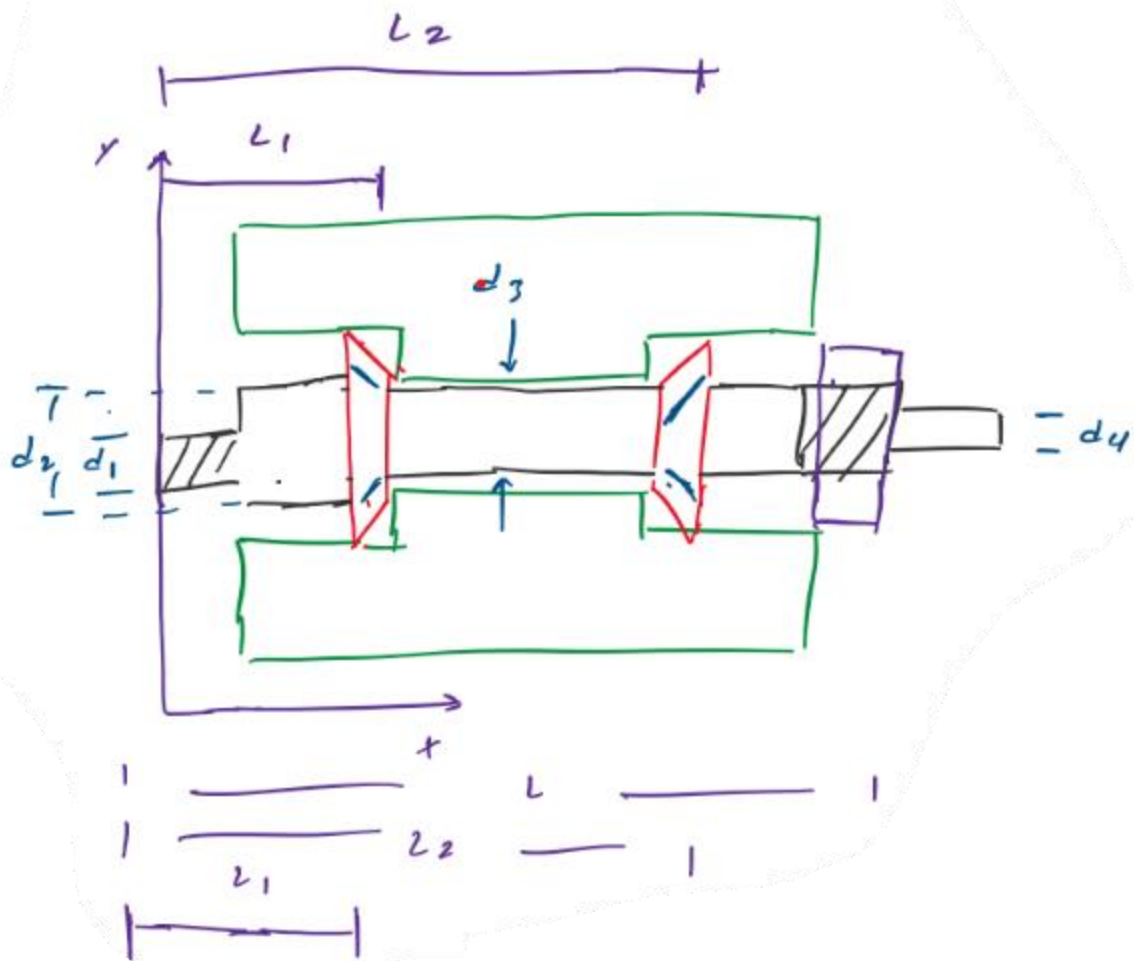


Figure A.3. Sketches of the shaft in x-y and x-z planes.

Reaction

$$\Sigma F_z = 0 = R_1 + R_2 - F_x - T$$

$$\Sigma M_y = 0 = R_1 L_1 + R_2 L_2 - T L$$

$$R_1 = \frac{T L - R_2 L_2}{L_1}$$

$$R_2 = F_x + T - R_1$$

$$R_1 = \frac{T L - (F_x + T - R_1) L_2}{L_1}$$

$$R_1 L_1 = T L - F_x L_2 - T L_2 + R_1 L_2$$

$$R_1 (L_1 - L_2) = T L - F_x L_2 - T L_2$$

$$R_1 = \frac{T L - F_x L_2 - T L_2}{(L_1 - L_2)}$$

$$R_1 = \frac{T(L - L_2) - F_e L_2}{(L_1 - L_2)}$$

$$R_2 = F_b + T - \frac{T(L - L_2) - F_e L_2}{(L_1 - L_2)}$$

$$C_{10} = R_{max} \left[\frac{L_{10} - L_{e0}}{10^6} \right]^{1/9}$$

Figure A.4. Image of bearing reaction calculations.

```
%% Given
f = 0.004; % in/rev
v_s = 600; % ft/min
alpha = 12:25;
len_alpha = length(alpha);
D = 1; % in

step = (0.4 - 0.15) / (14 - 1);
% u_s = 0.15:step:0.4; % hp * min/in^3
u_s = 0.4;
N = 1; % number of teeth

d = 0.01; % in
hp_to_psi = 3.96e5;
lbs_to_newtons = 4.4482216153;
mu = 0.5;
```

Figure A.5. Image of given variables for bearing selection calculations.

Appendix B

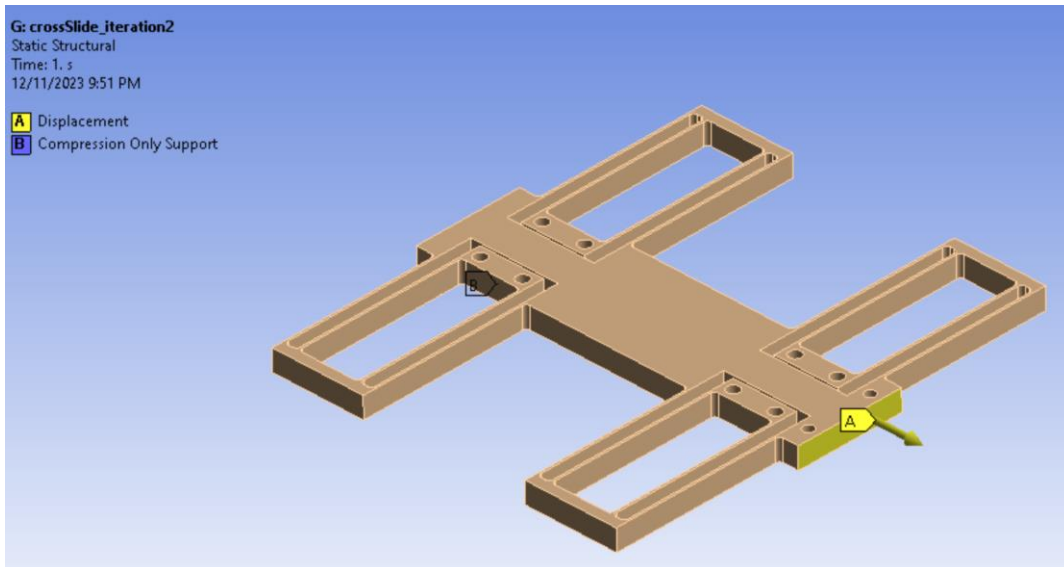


Figure B.1: Displacement loading condition for cross slide flexure.

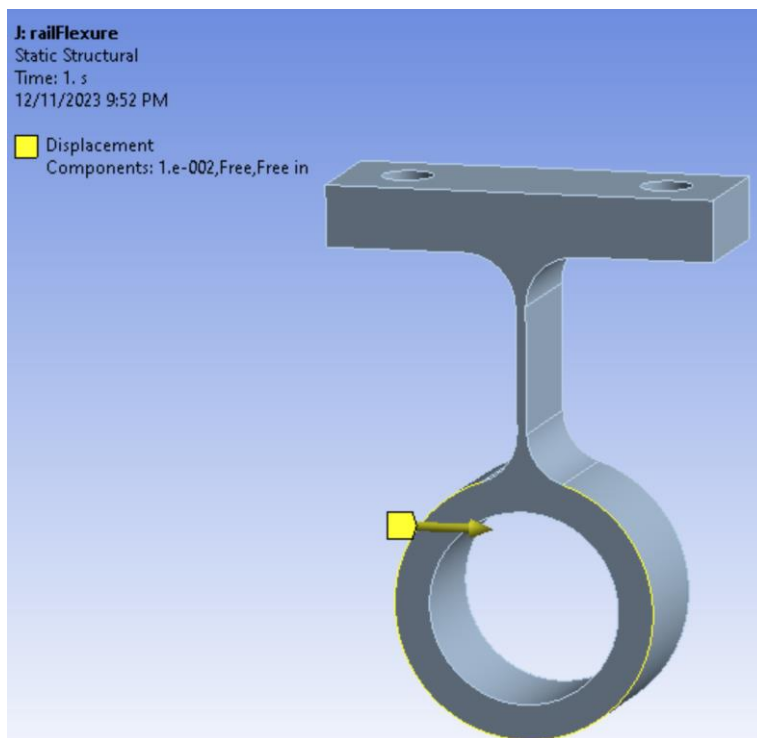


Figure B.2: Displacement loading condition for rail flexure.

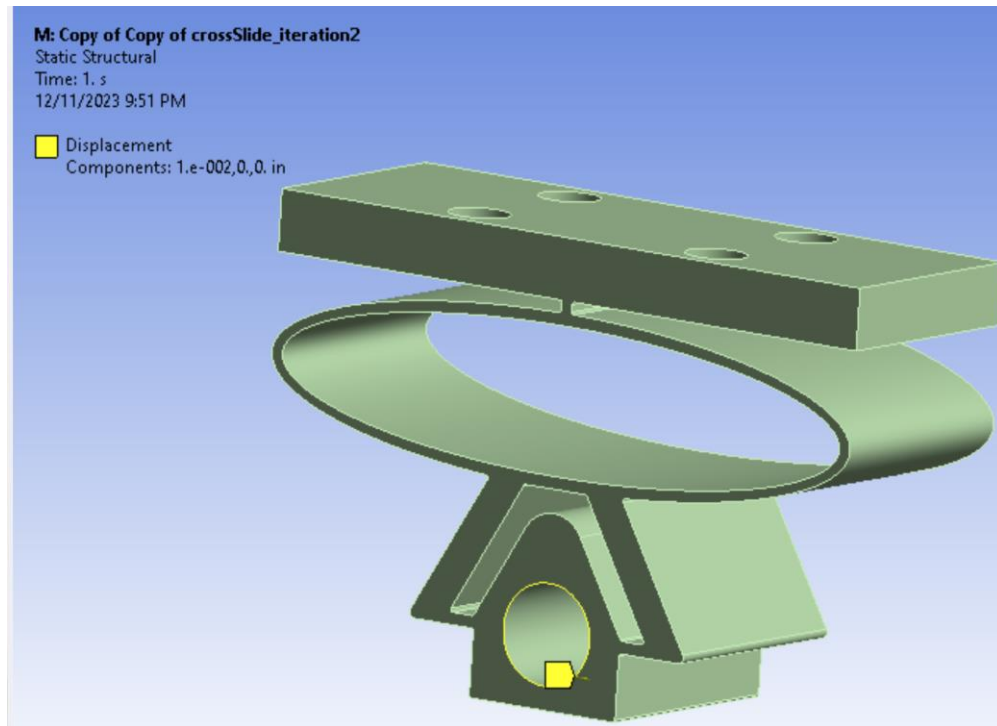


Figure B.3: Displacement loading condition for lead screw flexure.

Appendix C

```
%% Belt and Pulley
```

```
clear all;
```

```
format short g;
```

```
%% Given
```

```
n = 2291.8; % rpm
```

```
H_nom = 0.5;
```

```
d = 2.5;
```

```
D = 4.95;
```

```
L_out = 33;
```

```
t = (5/16);
```

```
L_A = 1.3;
```

```
n_d = 1;
```

```
K_s = 1.15; % service factor
```

```
K_c = 0.561;
```

```
%% Calculations
```

```
V = (d * n)/(3.82); = 1499.9 ft/min
```

```
L_in = L_out - 2 * t; = 32.375 in
```

```
L_p = L_in + L_A; = 33.675 in
```

```
C = 0.25 * ((L_p - (pi/2) * (D + d)) + ...  
    sqrt((L_p - (pi/2) * (D + d))^2 - 2 * (D - d)^2)) = 10.918 in
```

```
phi_d = pi - 2 * asin((D - d)/(2 * C)) = 2.9167°
```

```
ex = exp(0.5123 * phi_d); = 4.456
```

```
H_tab = (0.62 - 0.47) * (V - 1000)/(2000 - 1000) + 0.47; 6.545 hp
```

```
deg = (phi_d * 180)/pi; = 167.12°
```

$$K1 = (0.96 - 0.97) * (\text{deg} - 166.5) / (162.7 - 166.5) + 0.97; = 0.97162$$

$$K2 = 0.85;$$

$$H_a = K1 * K2 * H_{\text{tab}}; = 0.45 \text{ hp}$$

$$H_d = H_{\text{nom}} * K_s * n_d; = 0.575 \text{ hp}$$

$$N_b = H_d / H_a; = 1.2775$$

$$N_b = 1;$$

$$F_c = K_c * (V/1000)^2; = 1.262 \text{ lbf}$$

$$\text{deltaF} = (63025 * (H_d / N_b)) / (n * (d/2)); = 12.65 \text{ lbf}$$

$$F_1 = F_c + ((\text{deltaF} * e_x) / (e_x - 1)); = 17.573 \text{ lbf}$$

$$F_2 = F_1 - \text{deltaF}; = 4.923 \text{ lbf}$$

$$F_i = (F_1 + F_2) / 2 - F_c = 9.986 \text{ lbf}$$

$$n_{fs} = (H_a * N_b) / (H_{\text{nom}} * K_s) = 6.7827$$

Figure C.1. Image of MATLAB script calculations and numeric answers for the belt and pulley system.


```

% Bearing static load capacity
C_0 = 7400; %lb

k_bearing = 7400/(0.0001*0.305); %lb/in

bearing_1_deflection.x = 0;
bearing_2_deflection.x = 0;

bearing_1_deflection.y = -R1y/k_bearing;
bearing_2_deflection.y = -R2y/k_bearing;

bearing_1_deflection.z = -R1z/k_bearing;
bearing_2_deflection.z = -R2z/k_bearing;

%% HTMs: Unloaded Spindle Side

D_A = 5.813;
H_OA = [1 0 0 0;
        0 1 0 0;
        0 0 1 D_A;
        0 0 0 1];

H_AB = [1 0 0 L_hs-L1;
        0 1 0 0;
        0 0 1 0;
        0 0 0 1];

d_spindle2chuck = 0.29+1.5;
d_chuck2part = 1.04;
L_part = 1.25;

H_BC = [1 0 0 d_spindle2chuck;
        0 1 0 0;
        0 0 1 0;
        0 0 0 1];

H_CG = [1 0 0 d_chuck2part+L_part;
        0 1 0 -0.25;
        0 0 1 0;
        0 0 0 1];

```

```

H_unloaded{1} = H_OA;
H_unloaded{2} = H_OA*H_AB;
H_unloaded{3} = H_OA*H_AB*H_BC;
H_unloaded{4} = H_OA*H_AB*H_BC*H.CG;
H_OG = H_unloaded{4};

%% HTMs: Loaded Spindle Side
% FEA of headstock results
theta_OA.x = -3.05e-5;
theta_OA.y = -6.68e-5;
theta_OA.z = 5.92e-5;

delta_OA.x = -0.002;
delta_OA.y = 1.46e-5;
delta_OA.z = 1.552e-5;

H_A = HTM_3D_Rotation(theta_OA.x,theta_OA.y,theta_OA.z);
H_A_O = HTM_3D_Translation(delta_OA.x,delta_OA.y,D_A+delta_OA.z);
H_OA = H_A_O*H_A;

theta_AB.x = 0;
theta_AB.y = -asin((bearing_1_deflection.z-bearing_2_deflection.z)/d_bearings);
theta_AB.z = asin((bearing_1_deflection.y-bearing_2_deflection.y)/d_bearings);

delta_AB.x = 0;
delta_AB.y = bearing_1_deflection.y;
delta_AB.z = bearing_1_deflection.z;

H_B = HTM_3D_Rotation(theta_AB.x,theta_AB.y,theta_AB.z);
H_B_A = HTM_3D_Translation(L_hs-L1+delta_AB.x,delta_AB.y,delta_AB.z);
H_AB = H_B_A*H_A;

E_steel = 30e6;
E_aluminum = 10e6;

% H_BC
delta_BC.x = -1.03e-4;
delta_BC.y = 7.25e-5;
delta_BC.z = 2.94e-4;

theta_BC.x = -1.28e-6;
theta_BC.y = -4.48e-4;
theta_BC.z = 1.52e-4;

```

```

H_C = HTM_3D_Rotation(theta_BC.x,theta_BC.y,theta_BC.z);
H_C_B = HTM_3D_Translation(d_spindle2chuck+delta_BC.x,delta_BC.y,delta_BC.z);
H_BC = H_C_B*H_C;

% H_CG
delta_CG.x = 0;
delta_CG.y = 1.06e-4;
delta_CG.z = 4.09e-4;

H_CG = HTM_3D_Translation(d_chuck2part+L_part+delta_CG.x,-0.25+delta_CG.y,delta_CG.z);

H_loaded{1} = H_OA;
H_loaded{2} = H_OA*H_AB;
H_loaded{3} = H_OA*H_AB*H_BC;
H_loaded{4} = H_OA*H_AB*H_BC*H_CG;
H_OG_loaded = H_loaded{4};

spindle_error = H_OG_loaded - H_OG

%% Tool side
% I: Fixed support of tool
H_IG = [1 0 0 0;
        0 1 0 0.624;
        0 0 1 0;
        0 0 0 1];

% Cutting tool
% Cantilever model
l_tool = 0.624;
width_tool = 0.374;
I_tool = width_tool^4/12;

delta_ID.x = 0;
delta_ID.y = -F_t*l_tool/E_steel/width_tool^2;
delta_IG.z = -F_c*l_tool^3/3/E_steel/I_tool;

H_IG_loaded = HTM_3D_Translation(delta_ID.x,0.624+delta_ID.y,delta_IG.z);

M_c = -F_c*l_tool;

%% J: bottom of carriage
H_JI = [1 0 0 -0.19;
        0 1 0 -0.874;
        0 0 1 2.474;
        0 0 0 1];

```

```

delta_JI.x = 0;
delta_JI.y = -5.126e-6;
delta_JI.z = 0;

theta_JI.x = atan(0.003/9.06);
theta_JI.y = 0;
theta_JI.z = -atan((2.445e-6+1.303e-7)/9.06);

H_I = HTM_3D_Rotation(theta_JI.x,theta_JI.y,theta_JI.z);
H_I_J = HTM_3D_Translation(-0.19+delta_JI.x,-0.874+delta_JI.y,2.474+delta_JI.z);
H_JI_loaded = H_I_J*H_I;

H_OJ = [1 0 0 4.066;
        0 1 0 0;
        0 0 1 3.516;
        0 0 0 1];

delta_OJ.x = 0;
delta_OJ.y = -3.2e-4;
delta_OJ.z = -6.33e-4;

theta_OJ.x = -8.97e-5;
theta_OJ.y = 0;
theta_OJ.z = 0;

H_J = HTM_3D_Rotation(theta_OJ.x,theta_OJ.y,theta_OJ.z);
H_J_O = HTM_3D_Translation(delta_OJ.x+4.066,delta_OJ.y,3.516+delta_OJ.z);
H_OJ_loaded = H_J_O*H_J;

H_OG = H_OJ*H_JI*H_IG;

H_OG_loaded = H_OJ_loaded*H_JI_loaded*H_IG_loaded;
tool_error = H_OG_loaded-H_OG

%% Stiffness calcs
rail_D = 0.5;
I_rail = pi/64*rail_D^4;
E_rail = 30e6;
l_rail = 9.6;

x_load = 4.066;

K_rail = 6*E_rail*I_rail*l_rail^3 ...
        / (l_rail-x_load)^2/x_load^2/(x_load*(2*x_load+l_rail)-3*x_load*l_rail);

```

```

%% Lower Leadscrew
leadscrew_size = 0.5;
leadscrew_threadperinch = 13;

if isequal(leadscrew_threadperinch,13)
    A_t = 0.1419;
elseif isequal(leadscrew_threadperinch,20)
    A_t = 0.1599;
end

leadscrew_D = sqrt(A_t*4/pi);
I_leadscrew = pi/64*leadscrew_D^4;
E_leadscrew = 30e6;
l_leadscrew = 9.6;

x_load = 4.066;

K_leadscrew = 6*E_leadscrew*I_leadscrew*l_leadscrew^3 ...
    /(l_leadscrew-x_load)^2/x_load^2/(x_load*(2*x_load+l_leadscrew)-3*x_load*l_leadscrew);

```

Figure C.2. Image of MATLAB HTM script.

Appendix D

Table D.1 Runout Measurement Data

Degree	Output (μm) starting at 0°	Output (μm) starting at 180°
0	50.653	101.411
15	29.661	125.63
30	18.76	127.489
45	1.96	122.148
60	-16.216	108.412
75	-34.131	78.035
90	-53.014	44.938
105	-80.795	12.888
120	-96.166	-26.543
135	-105.229	-73.368
150	-103.767	-104.935
165	-89.231	-116.69
180	-60.447	-127.232
195	-29.847	-131.369
210	-7.607	-127.932
225	20.733	-114.332
240	49.959	-102.115
255	74.979	-83.828
270	88.314	-56.356
285	95.479	-30.766
300	97.274	-18.623

315	96.965	-1.707
330	92.28	14.87
345	73.439	60.391
360	52.445	101.418

```

import numpy as np
import matplotlib.pyplot as plt
import csv

data = []
# Open the file using with() and append each data point as a list into the data list.
with open('Runout Data.csv', 'r') as file:
    csvreader = csv.reader(file)
    for row in csvreader:
        data.append(row)

# Break out the values from the data list of lists:
deg_or = []
data0 = []
data1 = []
for row in data:
    if row[0] == 'i>θ':
        deg_or.append(float(θ))
    else:
        deg_or.append(float(row[0]))
        data0.append(float(row[1]))
        data1.append(float(row[2]))

# Convert from um to in:
for i in range(len(data0)):
    data0[i] = data0[i]/25400

for i in range(len(data1)):
    data1[i] = data1[i]/25400

# Average out the 0 and 180 data:
av = []
for i in range(len(data0)):
    av.append((data0[i] + data1[i])/2)

# Convert to an array for plotting:
av = np.asarray(av)

# Set the factor value for visualization of data:
factor = 50

# Make a new deg list in radians for plotting:
deg = np.linspace(0, 2*np.pi, 25)

# Calculate the radius for plotting:
r = 0.5 + av * factor

```

Figure D.1 Screenshot # 1 of the Runout Calculations Code from Python

```
# Plot the data:

fig, ax = plt.subplots(subplot_kw={'projection': 'polar'})
ax.plot(deg, r)
ax.set_rlabel_position(-22.5) # Move radial labels away from plotted line
ax.grid(True)

ax.set_title("Runout Error", va='bottom')
plt.show()
```

Figure D.2 Screenshot # 1 of the Runout Calculations Code from Python